energies

MDPI

Article

Vibration and Shock Mitigation on a Battery Pack Casing of an Electric Vehicle Using Mechanical Metamaterial and Biomimetic Structures

Yaocong Fan, Binjie Zhang, Hsiao Mun Lee * and Heow Pueh Lee

Department of Mechanical Engineering, National University of Singapore, 9 Engineering Drive 1, Singapore 117575, Singapore; e1520292@u.nus.edu (Y.F.); e1520199@u.nus.edu (B.Z.); mpeleehp@nus.edu.sg (H.P.L.)
* Correspondence: hmlee@nus.edu.sg

Abstract

This study investigates broadband vibration and mechanical shock mitigation for an aluminum (AlSi10Mg) battery pack casing by integrating mechanical metamaterial wall modifications and add-on damping structures. A 12.432 kWh underbody-type casing is designed. Two wall architectures, i.e., the star-triangular honeycomb (STH) and a novel hybrid auxetic (NHA), are implemented on three walls (top, front, and rear) of the battery pack casing. A mechanical damping (DSMS) and three biomimetic damping concepts (BWBIS, BPPIS and BBIGPS) are further compared. All designs are evaluated through simulation using random vibration analysis based on ISO 12405-2 standard, followed by shaker-based shock and random vibration experiments. Simulations show that both modified casings suppress the casing vibration by approximately 10^2–10^6 relative to the solid casing, and their dominant peaks shift to above 150 Hz. The NHA casing provides higher overall vibration mitigation than the STH casing (98.07% longitudinal, 95.09% vertical, and 93.60% transverse versus 97.64%, 94.00%, and 91.51%). Thus, the NHA casing is selected for fabrication. In addition, BPPIS and BBIGPS outperform BWBIS and DSMS, and thus, BPPIS is selected for fabrication due to its simpler geometry and lower mass. Experimentally, the solid-BPPIS configuration achieves the most robust random vibration attenuation across all measurement points, with average root mean square (RMS) reductions of 26.82% (vertical), 87.34% (longitudinal), and 83.60% (transverse). Shock tests reveal strong direction dependence; adding damping structures improves longitudinal and transverse shock mitigation, while vertical shock mitigation remains limited. The results provide design-level guidance on selecting wall architectures and damping layouts for practical vibration and shock protection of electric vehicle (EV) battery pack casings.

Keywords: battery pack; casing; shock; vibration; biomimetic

Check for updates

Academic Editor: Georg Frey

Received: 14 May 2026
Revised: 2 June 2026
Accepted: 9 June 2026
Published: 11 June 2026

Copyright: © 2026 by the authors. Licensee MDPI, Basel, Switzerland. This article is an open access article distributed under the terms and conditions of the Creative Commons Attribution (CC BY) license.

1. Introduction

Recent years have witnessed a rapid expansion of the EV and new EV markets, accompanied by a sharp increase in car battery deployment, where battery packs are commonly packaged as rectangular or T-shaped underbody modules to optimize center of gravity, cabin space utilization, and torsional rigidity [1,2]. However, this type of placement exposes battery packs to multi-source road-induced vibration and impact loads, which may exacerbate cell-level damage, accelerate degradation, and increase safety risks [3].

Over the past decade, metamaterials have attracted intense interest because their unusual properties are governed primarily by engineered architectures rather than constituent materials, initially defined as artificial media with unconventional electromagnetic responses [4]. The concept has evolved to encompass mechanical metamaterials whose tailored internal configurations deliver a broad range of functionalities [5], such as auxetic (negative Poisson's ratio, NPR) deformation, anomalous stiffness–density scaling [6], and high energy absorption [7]. In particular, auxetic mechanical metamaterials are appealing for structural protection under dynamic loading. Its representative families include classical re-entrant honeycombs [8], topology-optimized NPR architectures [9], star-shaped and novel partially-curved-beam hybrid auxetic (PCBHA) metamaterials with tunable auxeticity and improved energy absorption [10,11]. Despite these advances, their system-level integration into battery pack casings for broadband vibration mitigation under service-relevant excitations remains comparatively underexplored.

Rapid advances in bio-inspired architected structures have been seen in recent years, translating hierarchical principles from natural systems into lightweight, damage-tolerant lattices and composites via multiscale modeling, topology optimization, and advanced manufacturing [12]. Representative progress includes energy-absorbing bio-inspired metamaterials [13], nature-inspired hierarchical porous building materials that couple low carbon footprint with high strength and toughness [14]. Some emerging damping attenuation designs also appear, such as mussel byssal thread–inspired supramolecular elastomers [15] and cuttlefish bone-inspired microlattices, which enable broadband sound absorption with robust compressive response [16]. Nevertheless, relative to the extensive literature on quasi-static strengthening and single-event energy absorption, system-level vibration and shock mitigation under broadband, multi-source service excitations remain underexplored, motivating integrated design frameworks for real engineering housings.

To bridge the above gap, this work aims to mitigate the shock and vibration levels on the battery pack casings by integrating mechanical metamaterials and bio-inspired structures into the battery pack casing. Parametric structures are used to control vibration transmission and promote energy dissipation while preserving load-bearing capability and lightweight constraints. A unified dynamic evaluation framework is applied under a representative road spectrum to benchmark the power spectral density (PSD) responses and stress distribution at critical locations of the modified casings against a baseline casing. The results provide quantitative design guidelines for improving vibration suppression and shock tolerance in battery pack casings.

2. Methodologies

2.1. Design of the Battery Pack Casing

A battery pack casing with a total pack energy of 12.432 kWh is designed based on the battery cells from Grepow (NMC 811). The capacity and nominal voltage of each cell are 28 Ah and 3.7 V, respectively. The cells are arranged in a 3P40S configuration with a total cell number of 120. To ensure experimental safety and reduce testing costs, the Grepow NMC 811 cells are replaced by surrogate battery cells, which have closely matched geometry and mass with those of real battery cells. Compared to the real battery cells, the surrogate battery cells exhibited deviations of 0.2% in length, 1.5% in width, 4.7% in thickness, and 1.9% in mass. As illustrated in Figure 1a, each surrogate battery cell is fabricated by assembling two types of recycled polymer materials. The dimensions of the solid battery pack casing are shown in Figure 1b. The side wall thickness of the battery pack casing is 3.5 mm. The wall thicknesses of both the top cover and bottom base are 5 mm. These thicknesses are optimal for vibration-damping design [17].

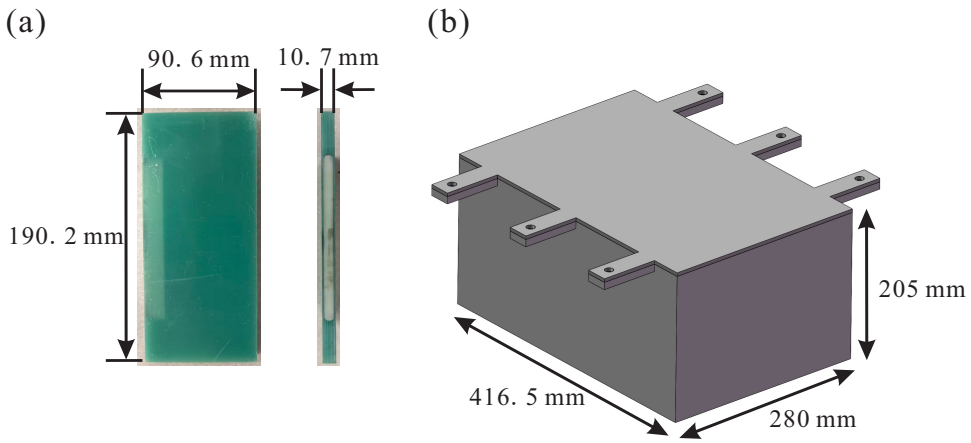

Figure 1. (**a**) Dimensions of the surrogate battery cell. (**b**) Overall dimensions of the solid battery pack casing [18].

2.2. Battery Pack Casing with Wall Modifications

The walls of the battery pack casings are modified using STH and NHA structures, as illustrated in Figure 2. In prior work [11], the baseline STH design [19] was further developed into the NHA configuration by introducing straight reinforcing rods, which led to increased mean stress, crushing force efficiency, and specific energy absorption under quasi-static compression. In the present study, both STH (see Figure 2a) and NHA (see Figure 2b) designs are systematically examined via shock and random vibration tests to assess whether the performance advantages reported under quasi-static loading still persist under dynamic operational conditions. To preserve global load-bearing capacity while enabling effective vibration mitigation, the metamaterial modifications are applied only to three walls (top, front, and rear) of the battery pack casing. The dimensions of the STH and NHA unit cells are summarized in Table 1.

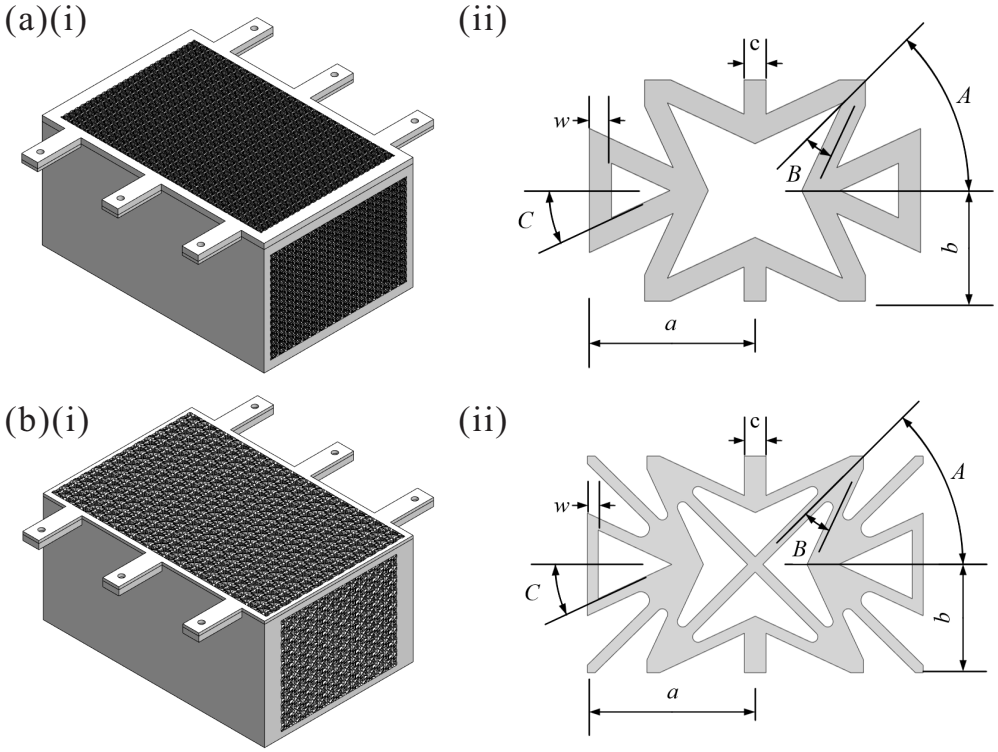

Figure 2. Battery pack casings with (**a**) STH [11] and (**b**) NHA [19] wall modifications.

Table 1. The dimensions of STH and NHA unit cells.

Structures	Dimensions						
	a	***b***	***c***	***w***	***A***	***B***	***C***
STH	7.5	5	2	1	45°	20°	45°
NHA	15.5	10	2	1	45°	20°	45°

Notes: The values of a, b, c and w are all in millimeters.

2.3. Damping Structures

2.3.1. Double-Strip Metamaterial Structure (DSMS)

A DSMS [20] is adopted for vibration isolation and shock attenuation by combining quasi-zero stiffness with snap-through buckling-induced energy dissipation (see Figure 3a). The DSMS unit cell (see Figure 3b) originates from a straight double-strip layout defined by a strip length $L = 80$ mm, strip spacing $S = 12$ mm, and out-of-plane thickness $t = 15$ mm. Rounded end corners ($r = 3$ mm) are introduced to trigger progressive inward buckling under compression. A thickness-asymmetric design ($t_1 = 0.6$ mm, $t_2 = 1$ mm) enforces a deterministic snap-through direction, where the thinner strip is constrained by the thicker one. Two such configurations are placed in parallel to form a unit cell with width $l = 80$ mm, platform height $h = 6$ mm, and spacing $d = 38.8$ mm. Multiple unit cells are then assembled in parallel to construct a DSMS block (see Figure 3c), with a central column of height 72 mm added for safety. The load capacity of one block, F, is evaluated from the material properties and geometry as

$$F = P_{t,0} + P_{T,0}, \tag{1}$$

$$P_{t,0} = n_0^2 E I_t, \tag{2}$$

$$P_{T,0} = n_0^2 E I_T, \tag{3}$$

where $P_{t,0}$ and $P_{T,0}$ denote the critical buckling forces of the thin and thick strips, respectively; $n_0 = 2\pi/L$; and I is the second moment of area where $I = bt^3/12$. Based on the supported mass and F, five DSMS blocks are used and evenly distributed to ensure uniform load sharing (see Figure 3d).

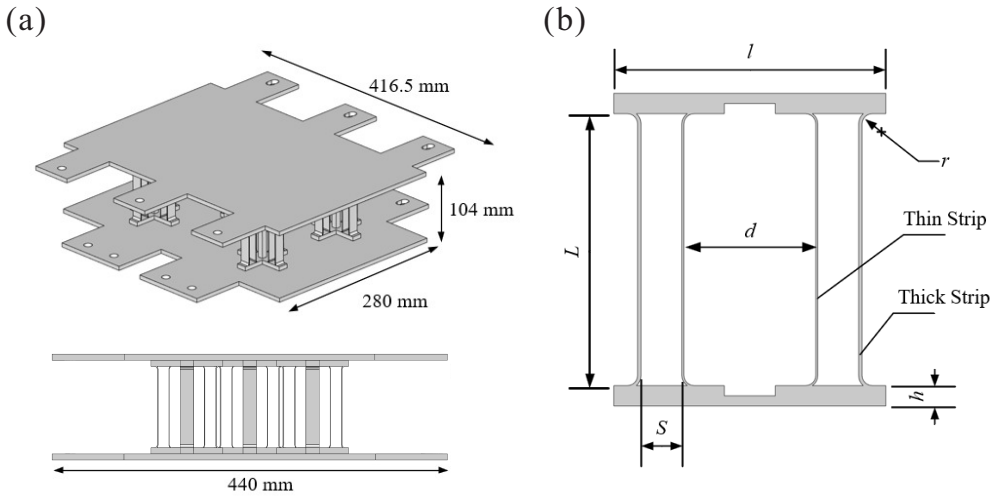

Figure 3. *Cont.*

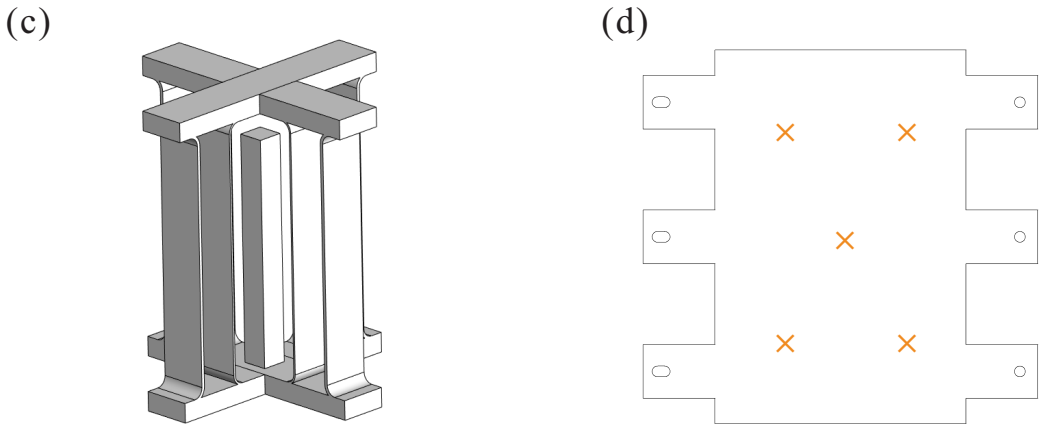

Figure 3. (**a**) DSMS with its (**b**) unit cell and its (**c**) unit block. (**d**) The positions of five unit blocks.

2.3.2. Biomimetic Bamboo-Inspired Gradient Porous Structure (BBIGPS)

To achieve vibration mitigation using a biomimetic structure, a graded porous structure is developed, inspired by the radially decreasing stiffness of natural bamboo [21,22], as shown in Figure 4a. Within a uniform cross-sectional domain, three layers of cavities with distinct sizes and spatial densities are embedded along the thickness direction to mimic the natural "stiff-to-soft" transition observed in bamboo [23]. The front layer (facing the excitation source) consists of 17 tightly packed rounded rectangles with width of 4 mm and length of 20 mm; the middle layer comprises 34 moderate size cylinders with radius of 5 mm; and the rear layer (farthest from the excitation) contains 17 sparsely distributed cylinders with radius of 6 mm, as shown in Figure 4b.

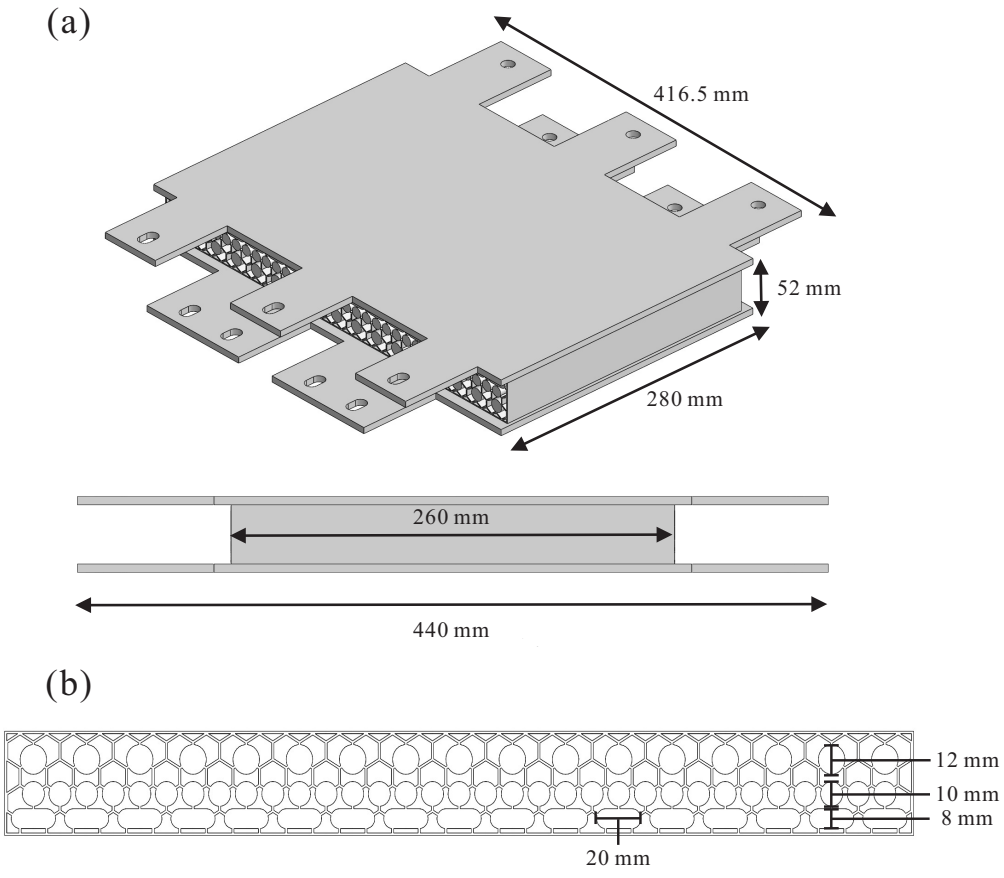

Figure 4. (**a**) BBIGPS with its (**b**) side view and dimensions of the cavities.

2.3.3. Biomimetic Woodpecker Beak-Inspired Structure (BWBIS)

The proposed vibration mitigation and energy dissipation structure is biomimetically derived from the corrugated, multilayered morphology and sutural-type interfaces of the woodpecker beak [24,25]. Such wave-like, overlapped structures are known to redistribute impact-induced stress waves and promote energy dissipation via interfacial mechanisms, enabling a favorable trade-off between load bearing and damping [26,27]. In this work, the unit profile is parameterized by a sinusoidal function with tunable amplitude (A_m) and wavelength (λ), generating periodic transverse corrugations that are stacked and arrayed along the longitudinal direction to form a multi-unit superposed configuration, as shown in Figure 5a. The sinusoidal geometry is defined by $A_m = 10$ mm as shown in Figure 5b. Following prior optimization studies on sinusoidal geometries, an intermediate amplitude ratio around 0.2 is frequently reported to yield near-optimal integrated performance for wavy profiles [28]. Accordingly, a moderate geometric steepness is adopted in the present design to balance deformation stability and dissipation capacity.

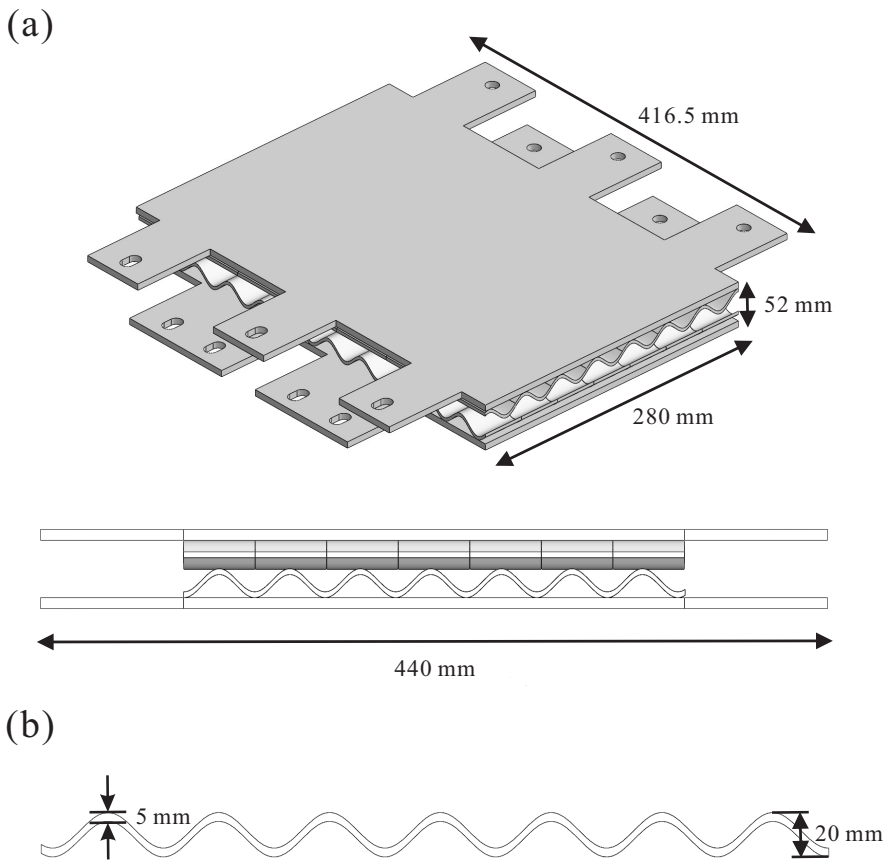

Figure 5. (**a**) BWBIS and its (**b**) unit cell dimensions.

2.3.4. Biomimetic Pomelo Peel-Inspired Structure (BPPIS)

Pomelo fruits can retain structural integrity even after falling from considerable heights, owing to the peel's outstanding cushioning and energy absorption capability [29]. This natural impact mitigation strategy motivates bio-inspired designs in which energy is dissipated through progressive local deformation. In particular, introducing secondary honeycomb units into conventional honeycomb cells to form hierarchical (nested) architectures enables stepwise, buckling-governed energy dissipation. A rotational honeycomb can be generated by imposing a prescribed twist angle (e.g., 30°) to incline the cell walls, thereby promoting a more uniform stress field and optimized collapse modes during compression, which substantially improves energy absorption efficiency [30]. Prior studies [31,32] have

further indicated that a configuration with three cells along each side of the honeycomb could achieve the highest specific energy absorption.

Based on these insights, a hybrid damping structure that integrates the pomelo peel-inspired hierarchical topology with rotational honeycomb units is developed, as shown in Figure 6a. The proposed design couples the stepwise buckling mechanism from hierarchical honeycombs with the multi-directional deformation from rotational units, thereby offering robust vibration and impact mitigation in both vertical and horizontal directions. To parameterize the layout and ensure geometric compatibility, the outer boundary is defined as a regular hexagon with a vertex-to-vertex distance $D = 50$ mm (see Figure 6d). The corresponding circumradius is $R = \frac{D}{2} = 25$ mm, side length is $S_l = R = 25$ mm, and apothem is $a_p = R\cos 30^\circ \approx 21.65$ mm. To accommodate a concentric circular inclusion while maintaining tangency with a surrounding ring of six identical regular hexagonal unit cells, a close-packed hexagonal tiling scheme is adopted. Specifically, six small regular hexagons (side length s) are arranged with 60° rotational symmetry about the center and are required to be mutually tangent to the outer hexagon as shown in Figure 6d. Under this constraint, the geometry is uniquely determined, yielding the scaling relation:

$$s = \frac{S_l}{3} \approx 8.33 \text{ mm}. \tag{4}$$

The central circle is tangent to the inner sides of the six surrounding hexagons; hence, its radius is:

$$r = \frac{\sqrt{3}}{2}s \approx 7.21 \text{ mm}, \tag{5}$$

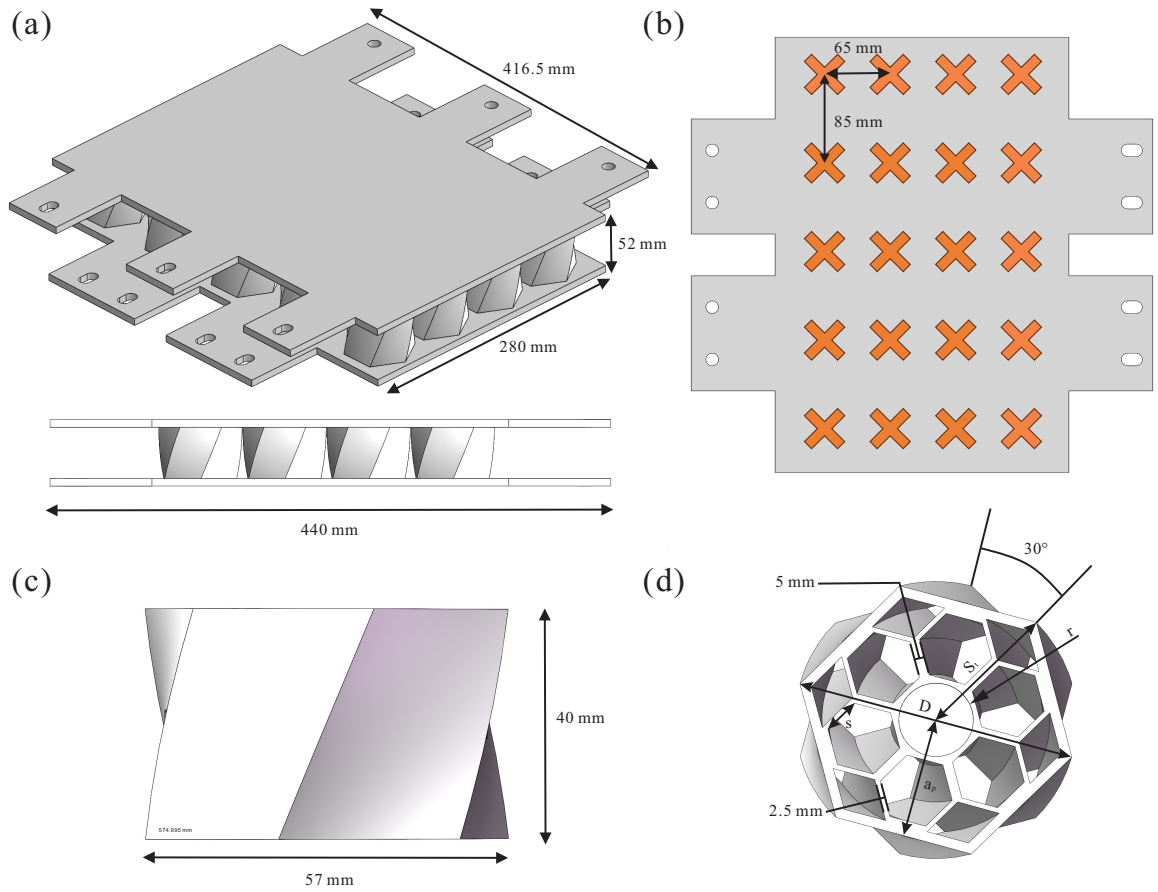

Figure 6. (**a**) BPPIS. (**b**) Arrangement of the BPPIS unit cells. (**c**) External dimensions of a unit cell. (**d**) Internal view showing wall thicknesses of 5 mm (center) and 2.5 mm (edge).

Compared with previously reported auxetic or honeycomb-inspired battery casing designs, the present work differs in both design philosophy and engineering validation. Previous studies have mainly focused on improving local energy absorption, crashworthiness, or stiffness-to-weight efficiency through periodic auxetic or honeycomb unit cells, often under quasi-static compression, simplified impact loading, or idealized boundary conditions. In contrast, this study evaluates a full aluminum battery pack casing under broadband random vibration and multi-directional shock excitation. This system-level evaluation is essential because the dynamic response of a practical battery casing is governed not only by the local deformation mechanism of the structural unit, but also by mounting constraints, interface conditions, and spatially varying response amplification. Therefore, the proposed NHA and BPPIS designs provide engineering advantages beyond conventional unit-cell-based auxetic or honeycomb concepts by combining casing-level load-path regulation with bottom-interface energy dissipation.

2.4. Numerical Setup

The simulation is conducted by Abaqus/CAE 2024 software. Only AlSi10Mg is simulated in this study, and the material properties of AlSi10Mg are summarized in Table 2 [33]. For capturing the simulation data, 25 reference points (RPs) are placed on the outer wall of the casing as shown in Figure 7. The x-axis, y-axis and z-axis are referred to as the longitudinal, vertical, and transverse directions, respectively. Four steps are created in the numerical model: modal analysis, x-longitudinal vibration, y-vertical vibration and z-transverse vibration [34]. The PSD profiles of the latter three steps are entered based on the data from ISO 12405-2 [35] and are shown in Tables A1–A3 in Appendix A. The total weight of the 120 units of battery cells is 46.44 kg, which is assigned as a uniformly distributed point mass in the numerical model. The cover and bottom parts of the casing are attached together by assigning a tie constraint between them. A pinned boundary condition is applied at the six bolt holes. In addition, the battery pack casing and the bottom damping structure are modeled as solid bodies and are connected using a tie constraint. The eight bolt holes of the damping structure are also assigned pinned boundary conditions. All boundary conditions are applied based on the actual experimental setup as shown in Figure 9.

Table 2. Material properties of AlSi10Mg (as-printed) [33].

Materials	Properties	Unit	Value
AlSi10Mg	Density (ρ)	kg/m^3	2700
	Poisson ratio (ν)	–	0.3
	Tensile strength (σ)	MPa	330
	Yield strength (σ_y)	MPa	210
	Hardness	HRC	75
	Elongation at break (A)	–	11%
	Young's modulus as-printed (E)	GPa	44

Figure 8 shows the frequency-dependent acceleration responses calculated using three mesh sizes of 0.04, 0.03, and 0.02, in order to evaluate the influence of mesh density on the simulation results. The results indicate that the acceleration response curves obtained with mesh sizes of 0.03 and 0.02 are highly consistent over the whole frequency range, especially in terms of the resonance frequency and peak acceleration response. Both meshes predict the main resonance peak at approximately 145 Hz, with nearly identical peak values and similar attenuation trends after the resonance region. In contrast, the coarser mesh size of 0.04 captures the overall response trend but significantly underestimates the peak acceleration amplitude, indicating that this mesh is insufficient to accurately resolve the

dynamic response near resonance. Therefore, considering both computational accuracy and computational cost, the mesh size of 0.03 is selected for the subsequent simulations. This mesh provides results close to those obtained using the finer 0.02 mesh, while avoiding the additional computational expense associated with further mesh refinement. The casing is discretized using 484,197 quadratic tetrahedral elements of type C3D10, while the damping structure is discretized using 119,854 linear hexahedral reduced-integration elements of type C3D8R.

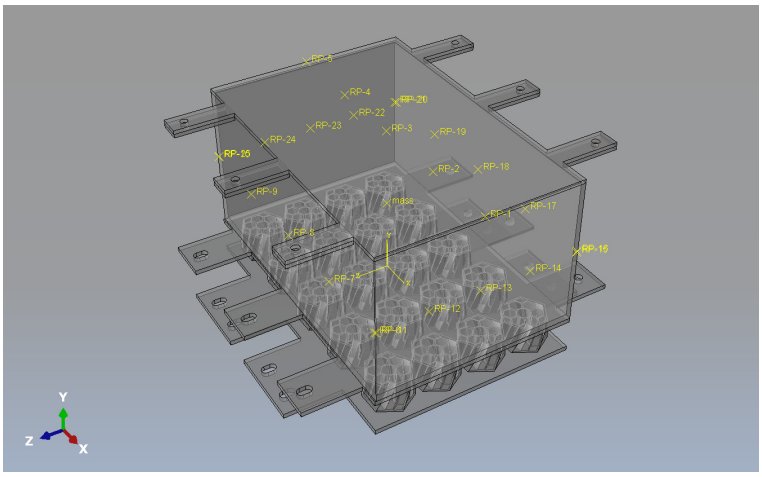

Figure 7. Numerical model of the present study. Only model with attached biomimetic pomelo peel structure is shown for brevity.

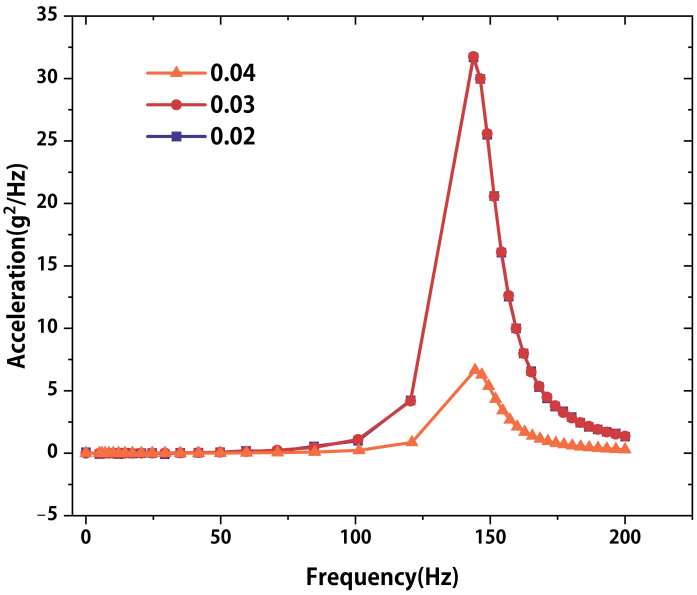

Figure 8. Mesh convergence analysis of acceleration response under different global mesh sizes.

2.5. Experimental Setup

The experimental setup employed in this study is illustrated in Figure 9. A STI electrodynamic shaker (model: DC-1000) is utilized to apply shock and random vibration inputs in accordance with the ISO 12405-2 standard [35] (see Tables A1–A4 in the Appendix A). The primary shock acceleration peak is configured at 76.52 m/s^2, determined based on the maximum force capacity of the STI shaker (F_c = 9800 N) [36]. Peak-to-peak displacements in the longitudinal, vertical and transverse directions are 2.2 mm, 3.7 mm, and 1.8 mm, respectively, which are obtained by integrating the PSD profiles from Tables A1 and A3.

Based on these values, the maximum testing frequency f is limited to 110 Hz using the following equations:

$$a = 0.002\, f^2\, d, \tag{6}$$

$$F_c = 1.2\, M\, a. \tag{7}$$

where a is the test acceleration, f is the frequency, d is the displacement, M represents the total mass (including test platform, battery pack casing, damping structure, surrogate battery cells, and all fixtures), and 1.2 is the applied safety factor.

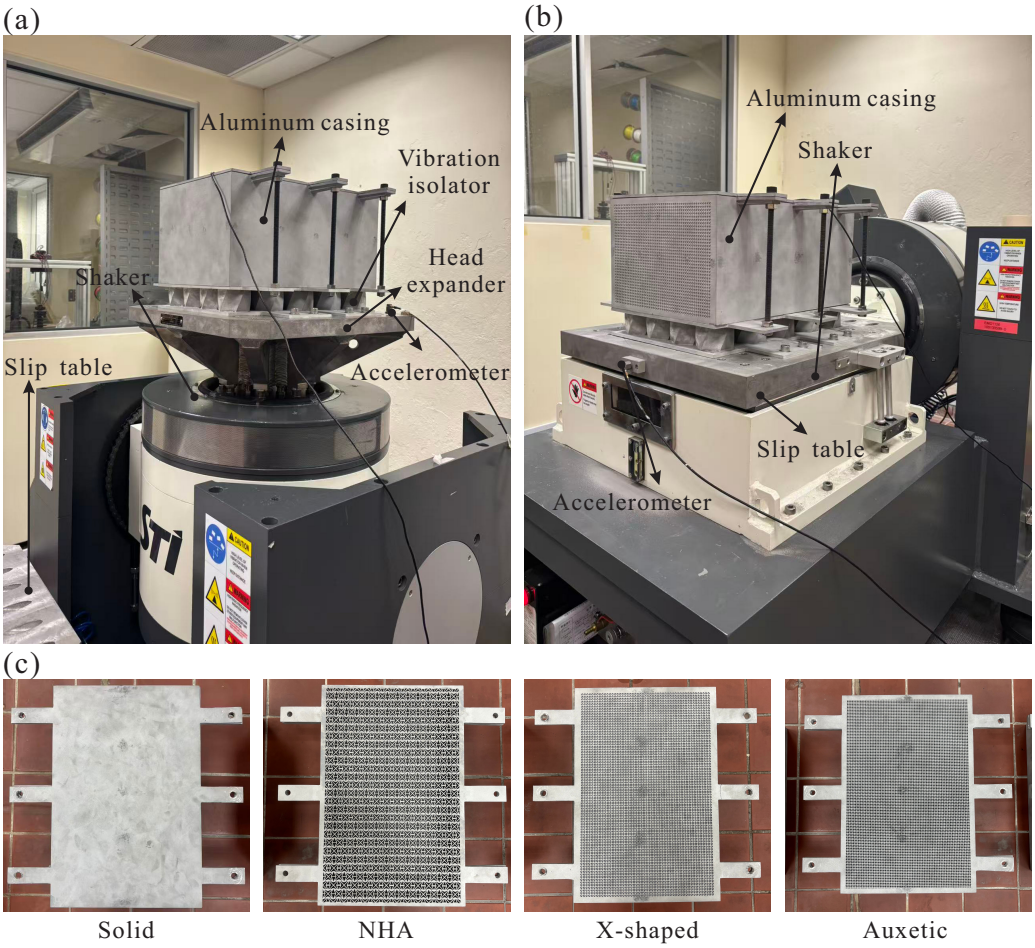

Figure 9. Experimental setup for (**a**) the vertical vibration test and (**b**) the longitudinal and transverse vibration tests. (**c**) Battery pack casings, including the solid, NHA, X-shaped, and auxetic configurations.

The STI head expander (model: TBS-500-150M) is employed for vertical vibration tests (see Figure 9a), while the STI slip table (model: SV-0505) is used for longitudinal and transverse vibration tests (see Figure 9b). The selected battery pack casing (NHA) and damping structure (BPPIS) are fabricated via 3D printing using aluminum. The material properties of AlSi10Mg are summarized in Table 2 [33]. Masses of all relevant experimental components are summarized in Table 3. For comparison, vibration and shock tests are also conducted on battery pack casings with auxetic and X-shaped wall modifications. The details of these two casings can be found in Wei et al. [18]. All vibrational data are collected using a Dytran single-axis IEPE accelerometer (model: 3055D1T) mounted on the surface of the battery pack casing. Vertical shock and vibration are measured from reference points RP1 to RP5, longitudinal shock and vibration from RP11 to RP15 and RP21 to RP25, and transverse shock and vibration from RP6 to RP10 and RP16 to RP20. Each measurement point is sampled for 1.5 min.

Table 3. The weights of all structures that have been used in the shock and vibration experiments.

Structures	Weight (g)
Aluminum solid battery pack casing	6250.0
Aluminum auxetic battery pack casing	5214.0
Aluminum X-shaped battery pack casing	4616.0
Aluminum NHA battery pack casing	4616.0
Aluminum BPPIS	4760.0
Surrogate battery cell	386.0

3. Results and Discussion

3.1. Simulation Results

3.1.1. Casing Simulations

The simulations are first used to investigate the vibration mitigation performance of the two designed casings. Figure 10 presents the acceleration responses in three directions of three aluminum casings at 45 Hz and 85 Hz. These two frequencies are shown because the dominant acceleration peaks of the solid casing in the three directions occur in these frequency ranges (see Figures 11–13). As shown in Figure 10, under identical contour limits and the same deformation scale factor, the deformation mode observed in the solid aluminum casing is not present in either the NHA or STH casing. The acceleration responses of reference points located at the wall center of the casings are presented from Figures 11–13. Results from all 25 reference points are not shown because RP6–RP10 are symmetric to RP16–RP20, and RP11–RP15 are symmetric to RP21–RP25. The vibration levels of the NHA and STH casings are approximately 10^2 to 10^6 times lower than that of the solid aluminum casing; thus, their results are plotted separately and shown in the insets of Figures 11–13. For both modified casings, the dominant acceleration peaks at all reference points occur above 200 Hz, indicating that resonance is unlikely under typical road-excitation frequencies.

To further quantify the vibration mitigation efficiency, the RMS value is used as a performance metric. The RMS at each RP is calculated using Equation (8):

$$\mathrm{RMS} = \sqrt{\int \mathrm{PSD}(f)\,\mathrm{d}f} \tag{8}$$

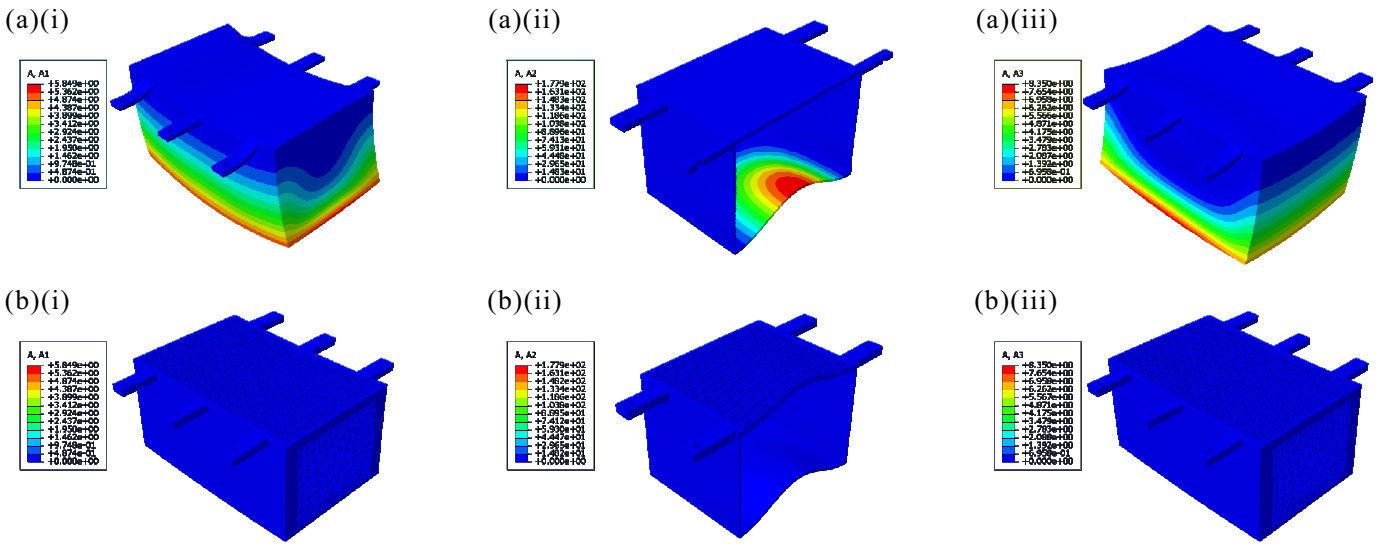

Figure 10. *Cont.*

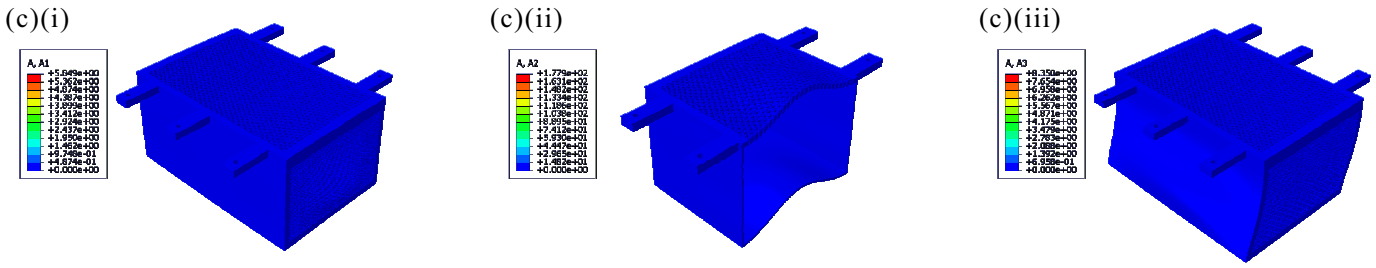

Figure 10. Acceleration contours of the aluminum (**a**) solid, (**b**) NHA and (**c**) STH battery pack casings. ((**i**)–(**iii**)) represent longitudinal acceleration at 85 Hz, vertical acceleration at 45 Hz and transverse acceleration at 85 Hz, respectively.

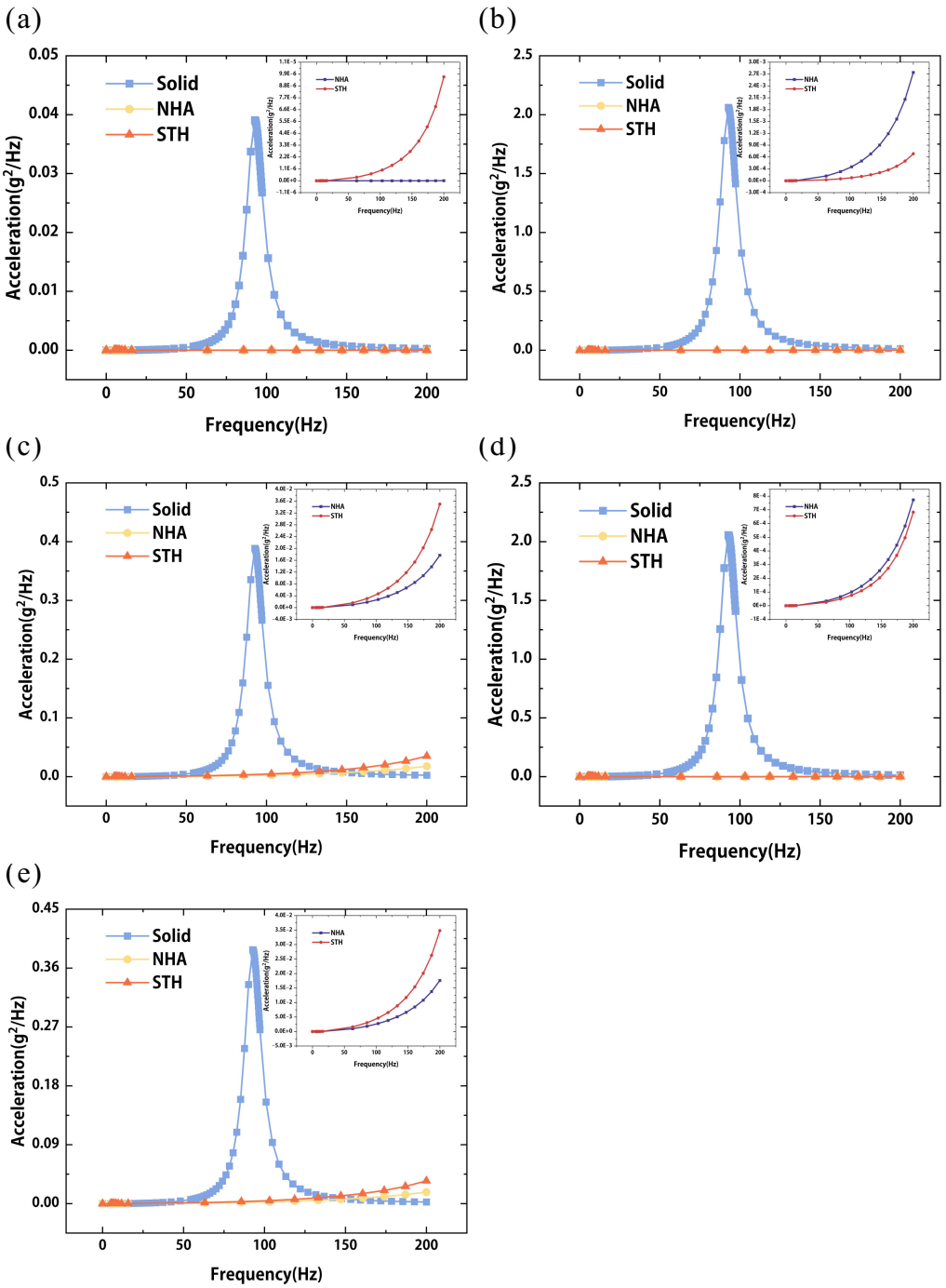

Figure 11. Longitudinal acceleration of the three different aluminum battery pack casings at (**a**) RP3, (**b**) RP8, (**c**) RP13, (**d**) RP18, and (**e**) RP23.

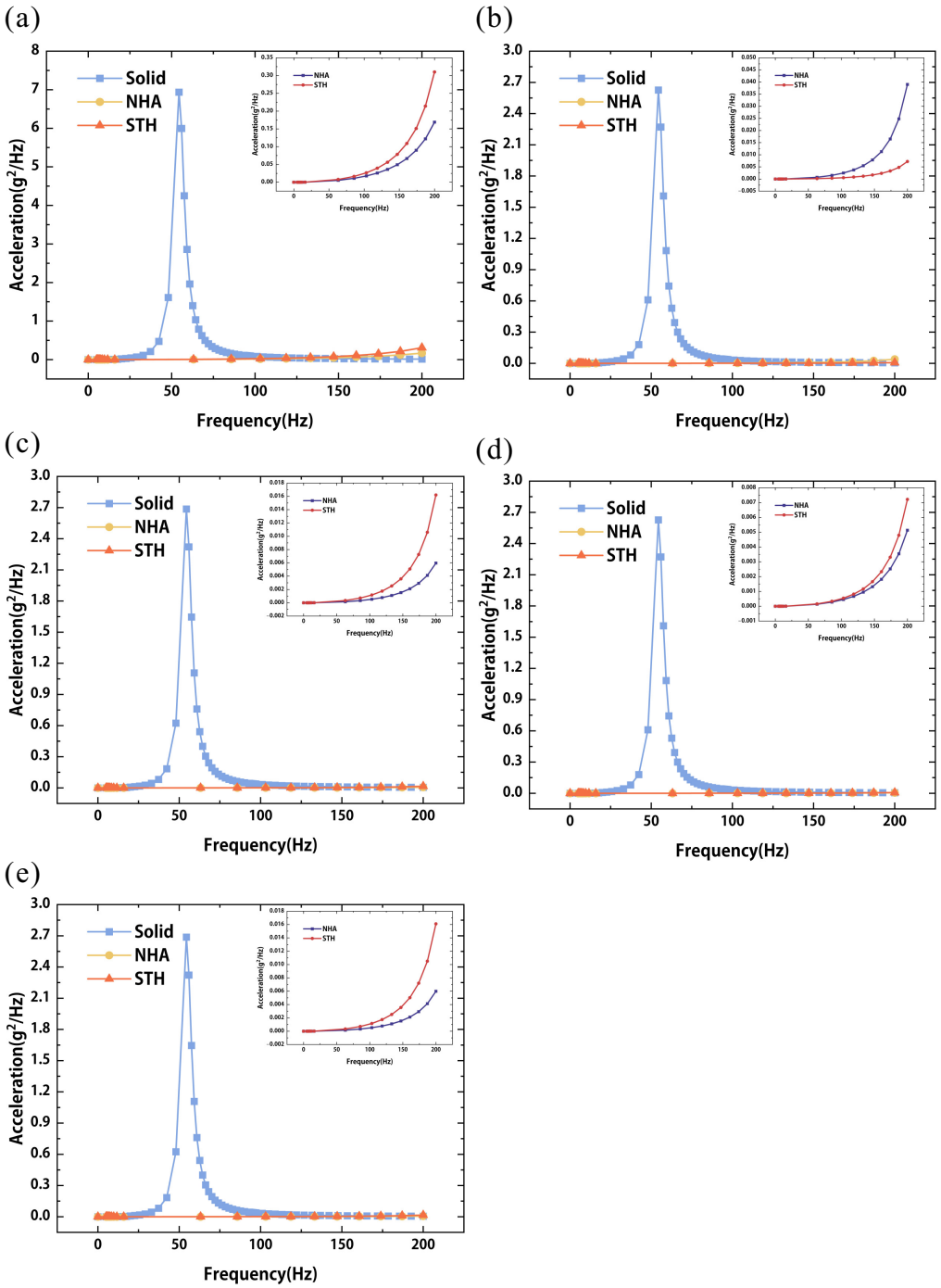

Figure 12. Vertical acceleration of the three different aluminum battery pack casings at (**a**) RP3, (**b**) RP8, (**c**) RP13, (**d**) RP18, and (**e**) RP23.

The vibration mitigation ratio of the NHA and STH casings at each RP is then computed as

$$\eta = \frac{\mathrm{RMS}_{\mathrm{solid}} - \mathrm{RMS}_{\mathrm{modified}}}{\mathrm{RMS}_{\mathrm{solid}}} \tag{9}$$

where $\mathrm{RMS}_{\mathrm{solid}}$ is the RMS of the solid casing and $\mathrm{RMS}_{\mathrm{modified}}$ is the RMS of the NHA or STH casing. The results are summarized in Table 4. Since the NHA casing shows higher mitigation ratios than the STH casing in all three directions, the NHA aluminium casing is selected for fabrication and the subsequent experiments.

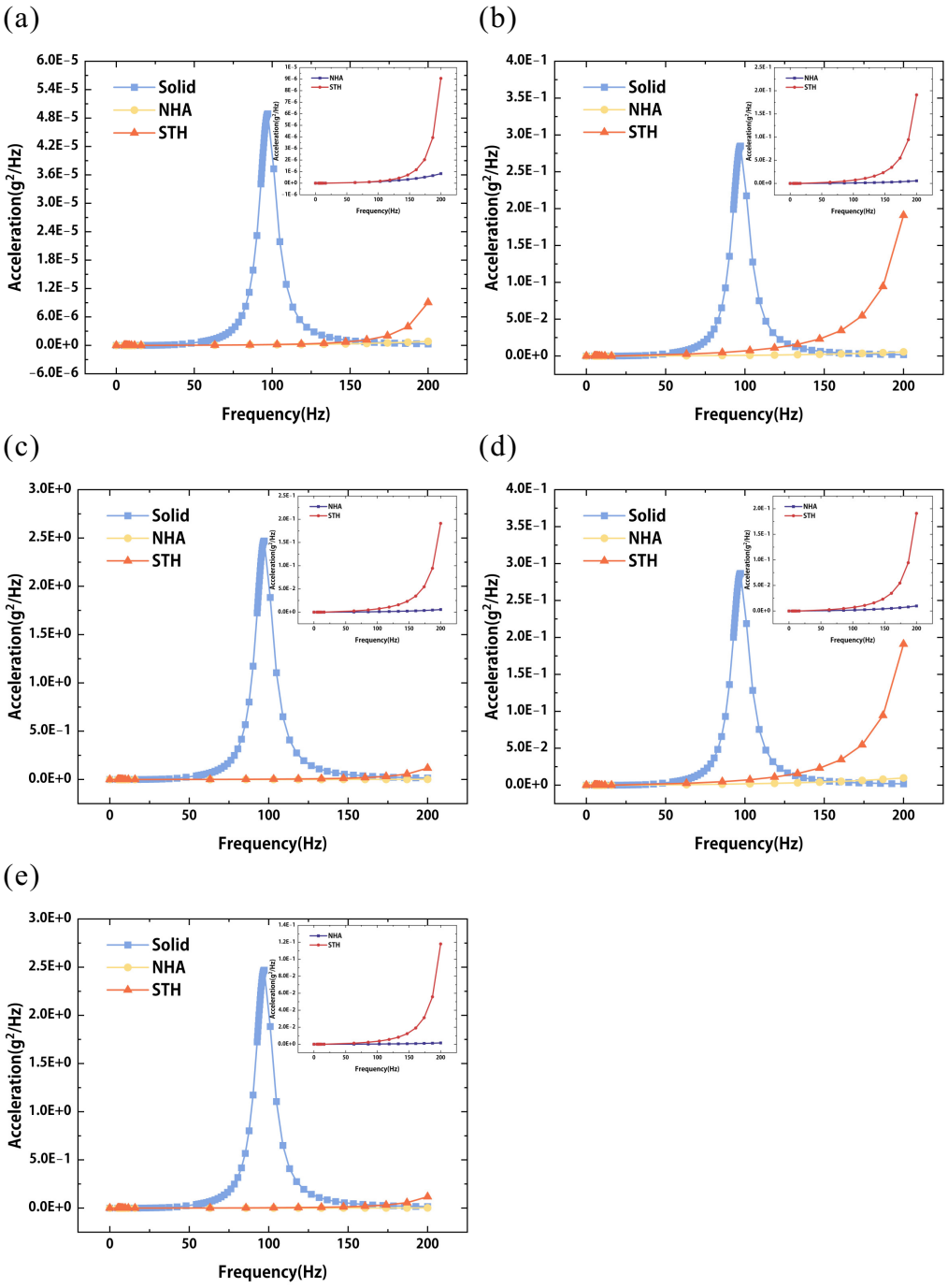

Figure 13. Transverse acceleration of the three different aluminum battery pack casings at (**a**) RP3, (**b**) RP8, (**c**) RP13, (**d**) RP18, and (**e**) RP23.

Table 4. Vibration mitigation capabilities of the aluminum NHA and STH battery pack casings in three directions.

Modified Battery Pack Casing	Longitudinal (%)	Vertical (%)	Transverse (%)
NHA	98.07	95.09	93.60
STH	97.64	94.00	91.51

3.1.2. Damping Structure Simulations

The vibration mitigation performances of four designed damping structures: BWBIS, BPPIS, BBIGPS, and DSMS are also evaluated using simulations. Figures 14–16 show the acceleration contours of the four designs in longitudinal, vertical, and transverse directions

at 152 Hz, 50 Hz, and 160 Hz, respectively. These frequencies are selected based on the peak acceleration of the DSMS in each direction (see Figures 17–19), because DSMS exhibits the poorest vibration mitigation performance among the four designs. The contour limits of the solid casing with attached DSMS in the longitudinal and transverse directions (see Figures 14d and 16d) are different from those of the other three damping structures because the DSMS has a much higher level of acceleration. In longitudinal and transverse directions, BWBIS, BPPIS, and BBIGPS exhibit a clear reduction in vibration response. In contrast, although DSMS shows a substantial reduction in acceleration, the deformation initiates within the damping structure (see Figure A1 in the Appendix A), may cause premature failure of the damping structure, and is therefore undesirable for practical vibration mitigation.

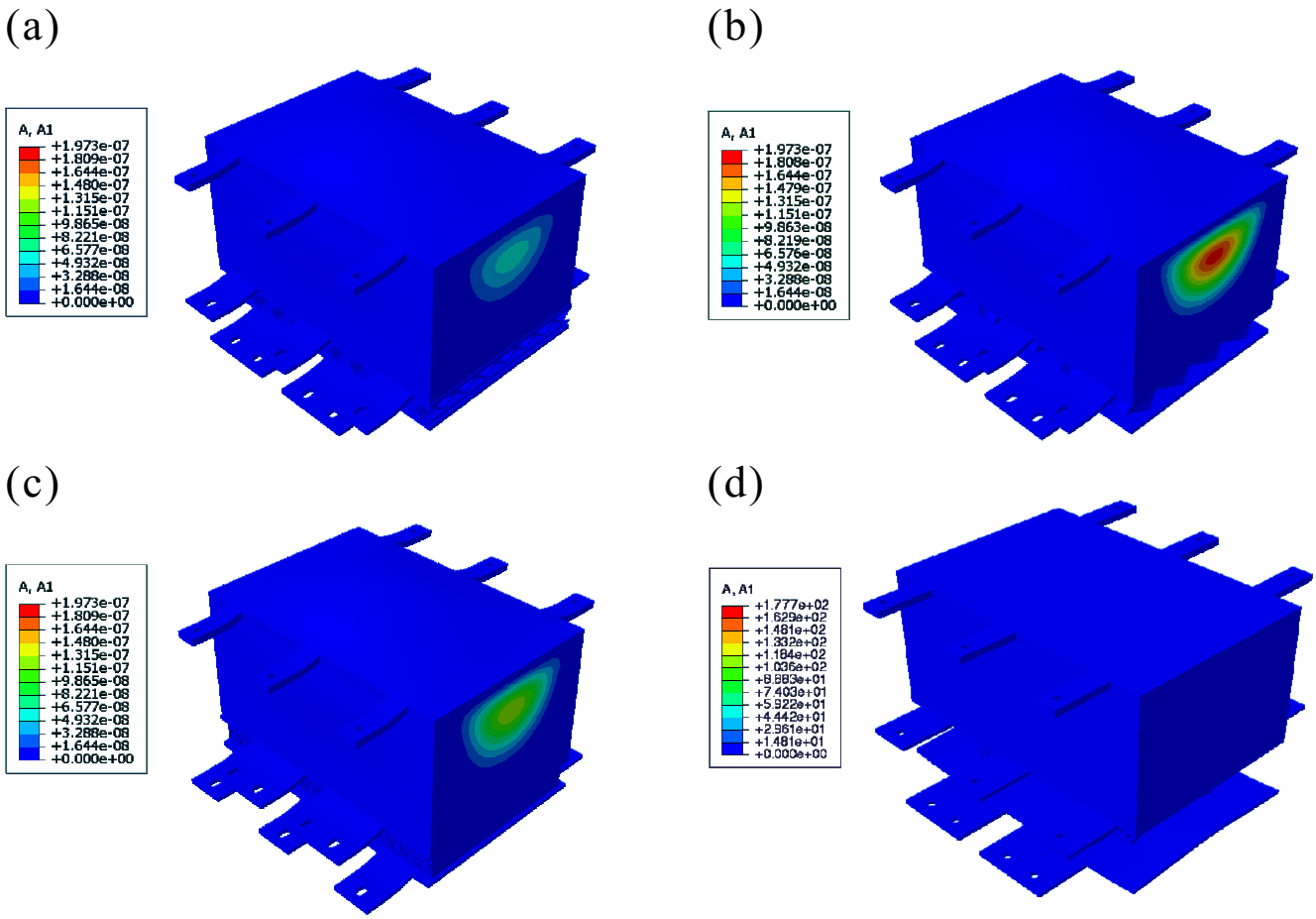

Figure 14. Longitudinal acceleration contours (152 Hz) of the aluminum solid battery pack casing with different damping structures. (**a**) BWBIS (**b**) BPPIS (**c**) BBIGPS (**d**) DSMS.

The vertical direction results (see Figure 15) show an opposite trend: the casings with damping structures exhibit lower mitigation performance than the solid casing without the damping structure (see Figure 15e different damping structures). This behavior is not unexpected in a random vibration (PSD-based) analysis, because introducing an additional structural component does not necessarily reduce the vibration response in all directions. Instead, it can redistribute the dynamic stiffness, shift resonance frequencies, and modify load-transfer paths, which may increase the response in a specific direction or at a specific location. In the present model, this vertical amplification is mainly attributed to the connection and boundary condition design of the damping structure. The damping structure is firmly connected to the casing via the constraint boundary condition, relative motion at their interface is not allowed. Therefore, the added damping structure cannot

provide effective energy dissipation mechanisms in the vertical direction, such as viscoelastic losses [37] and frictional sliding [38]. In addition, the constraints applied to the damping structure can make it deform more easily in local bending, which increases its contribution to the vertical vibration response within the PSD excitation band. Under random base excitation, the resulting changes in mode shapes and natural frequencies may concentrate the vertically dominated responses in frequency regions that are more strongly excited, which transfer additional inertial forces back to the casing through the rigid connection.

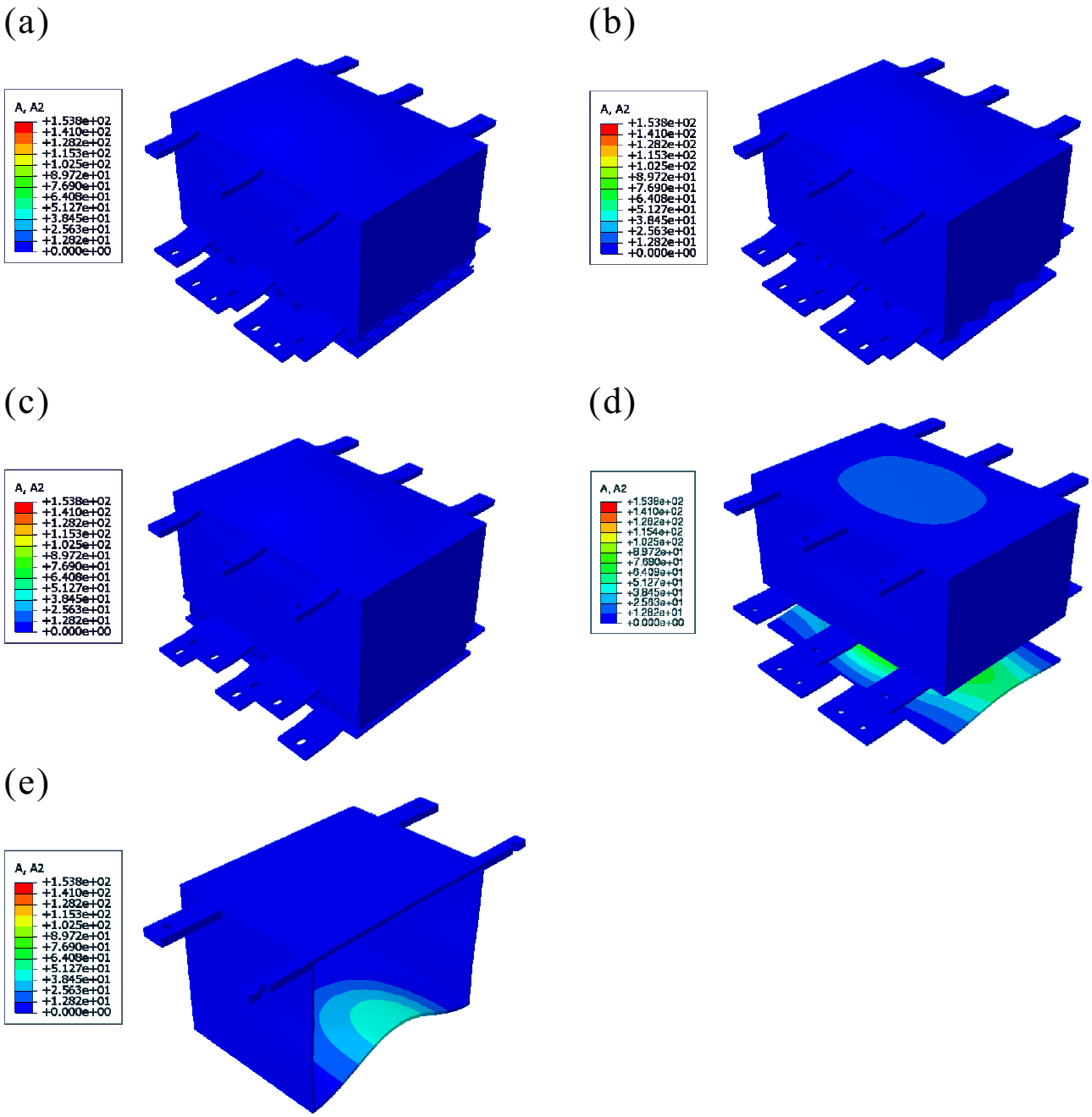

Figure 15. Vertical acceleration contours (50 Hz) of the aluminum (**e**) solid battery pack casing with different damping structures. (**a**) BWBIS (**b**) BPPIS (**c**) BBIGPS (**d**) DSMS.

Table 5 summarizes the vibration mitigation performance of the four damping structures based on Equation (9). BPPIS and BBIGPS show better mitigation performance than BWBIS and DSMS. Between BPPIS and BBIGPS, BPPIS has a simpler geometry and is easier to manufacture. It is also lighter and its weight is under the maximum payload limit

of the vibration shaker. Therefore, BPPIS is selected for fabrication and the subsequent experimental validation.

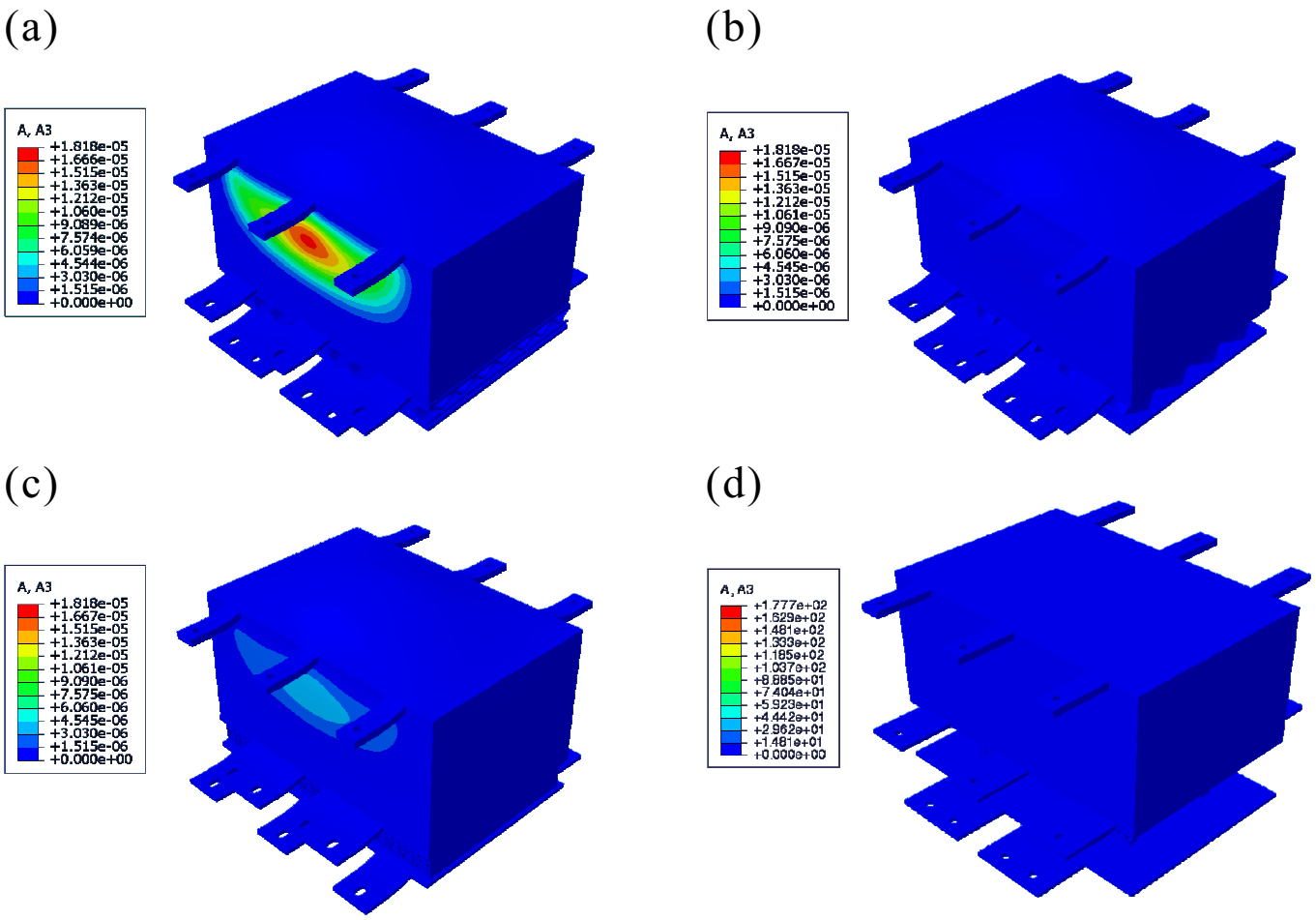

Figure 16. Transverse acceleration contours (160 Hz) of the aluminum solid battery pack casing with different damping structures. (**a**) BWBIS (**b**) BPPIS (**c**) BBIGPS (**d**) DSMS.

Table 5. Vibration mitigation capabilities of the aluminum solid battery pack casing with different damping structures in three directions.

Damping Structure	Longitudinal (%)	Vertical (%)	Transverse (%)
BPPIS	99.99	−92.84	99.78
BWBIS	99.98	−88.48	99.96
BBIGPS	99.99	−89.29	99.87
DSMS	74.46	−2.46	99.89

3.2. Experimental Results

3.2.1. Shock Experiment

The shock test results are shown in Table 6. The damping capability at each measurement point is determined by comparing the RMS values of the casing responses with and without target configuration. Specifically, taking the solid casing without any damping treatment or wall modification as the baseline, the damping capability of a given case can be calculated by Equations (8) and (9). A comparison between the NHA and auxetic designs shows that their shock mitigation performance is direction-dependent. Without additional damping structures, the auxetic casing performs better in the vertical and transverse directions, with positive shock mitigation at 60% and 80% of the measurement points, respectively, compared with 0% and 70% of the NHA casing. In contrast, the NHA casing

performs better in the longitudinal direction, where 60% of the measurement points show positive shock mitigation, compared with 30% of the auxetic casing. When BPPIS is added, both designs exhibit clear improvement in the longitudinal and transverse directions. For the NHA design, the proportion of measurement points with positive shock mitigation increases from 60% to 90% in the longitudinal direction and from 70% to 100% in the transverse direction, while no improvement is observed in the vertical direction (0% in both cases).

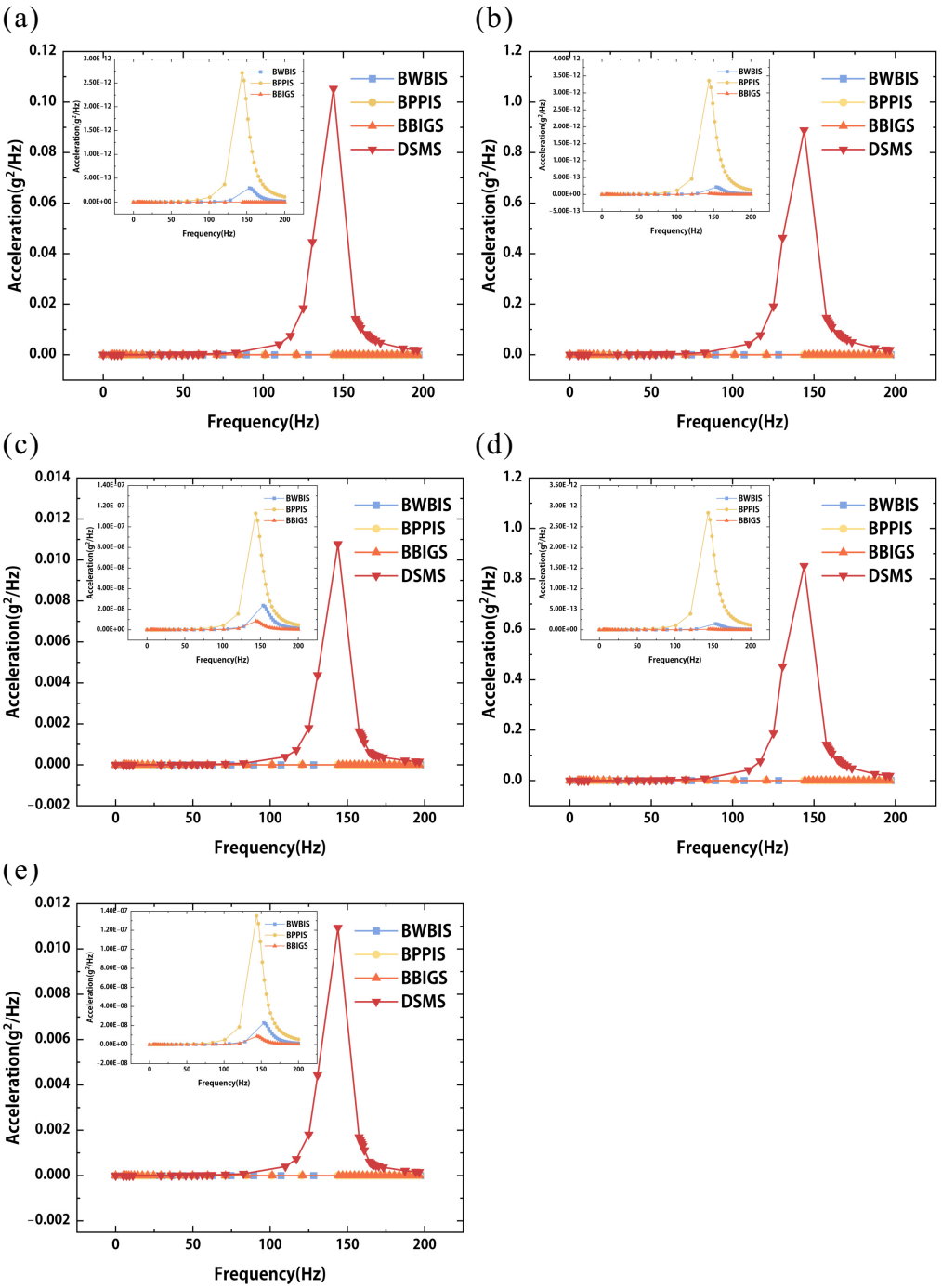

Figure 17. Longitudinal acceleration of the aluminum solid battery pack casing with different damping structures at (**a**) RP3, (**b**) RP8, (**c**) RP13, (**d**) RP18, and (**e**) RP23.

For the auxetic design, the addition of the BPPIS increases the corresponding values from 30% to 90% in the longitudinal direction and from 80% to 100% in the transverse direction. However, the vertical shock mitigation capability decreases from 60% to 0%. Overall, the BPPIS improve shock mitigation primarily in the longitudi-

nal and transverse directions, whereas their benefit in the vertical direction is limited under the present design and loading conditions. The maximum shock mitigation values are observed in the transverse direction, i.e., RP 19 (61.47%) for the NHA casing, RP 19 (85.87%) for the NHA-BPPIS, RP 18 (42.17%) for the auxetic casing, and RP 17 (96.01%) for the auxetic-BPPIS.

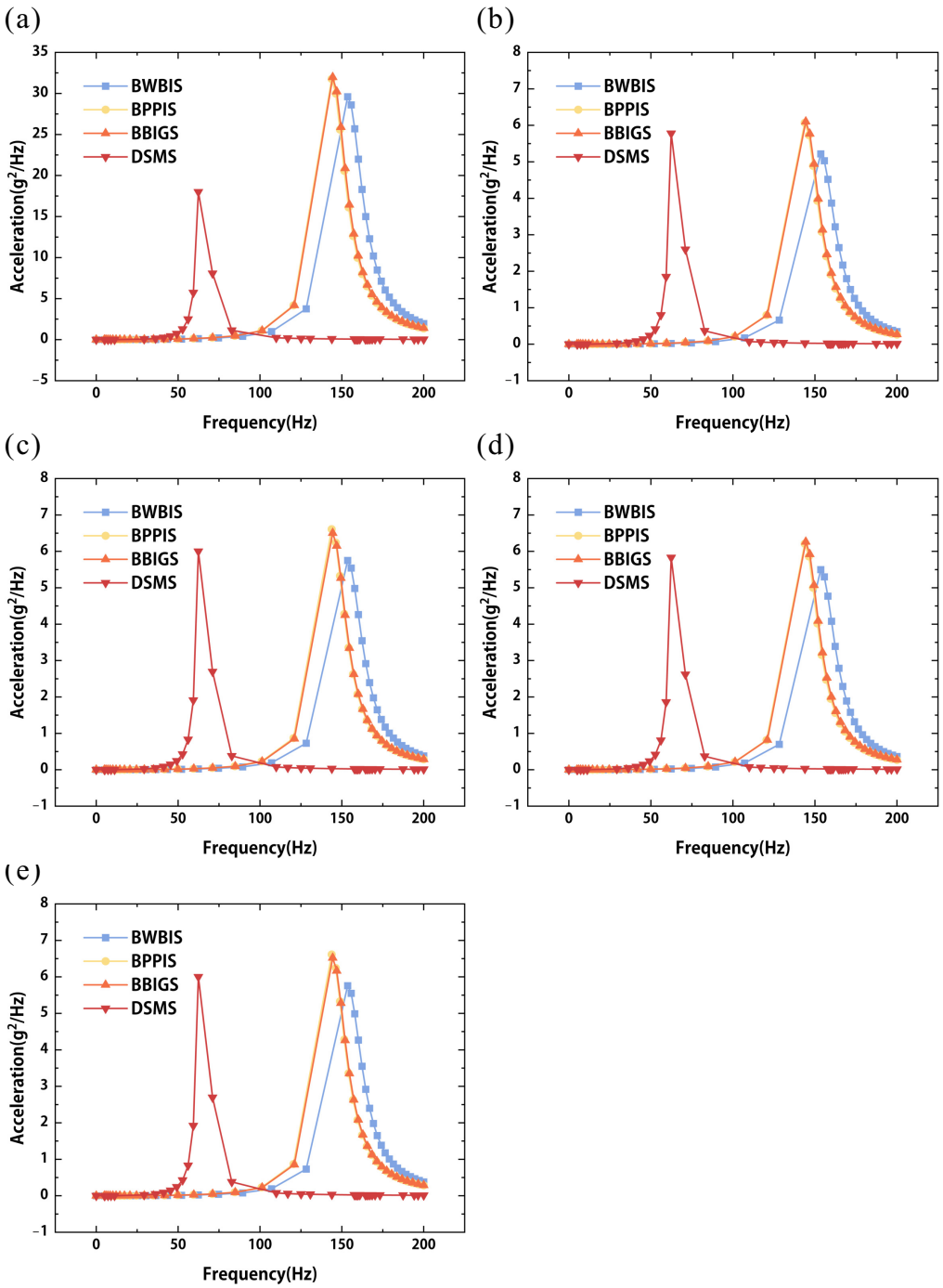

Figure 18. Vertical acceleration of the aluminum solid battery pack casing different damping structures at (**a**) RP3, (**b**) RP8, (**c**) RP13, (**d**) RP18, and (**e**) RP23.

3.2.2. Vibration Experiment

The vibration reduction capabilities of the aluminum battery pack casings with different wall designs and bottom damping configurations are summarized from Tables 7–9 (corresponding acceleration results are shown from Figures 20–22). It should be noted that RP11–RP15 and RP21–RP25, as well as RP6–RP10 and RP16–RP20, are symmetric

measurement sets. Therefore, for brevity, only the results of RP11–RP15 and RP6–RP10 are presented in this study. Overall, the solid-BPPIS configuration shows the most consistent and prominent vibration attenuation performance. It achieves an average reduction of approximately 26.82% in the vertical direction (RP1–RP5), and exceptionally high average reductions of 87.34% and 83.60% in the longitudinal and transverse directions, respectively. These results indicate that the bottom damping treatment dominates the energy dissipation process under this loading condition, likely through enhanced deformation/frictional dissipation within the damping layer.

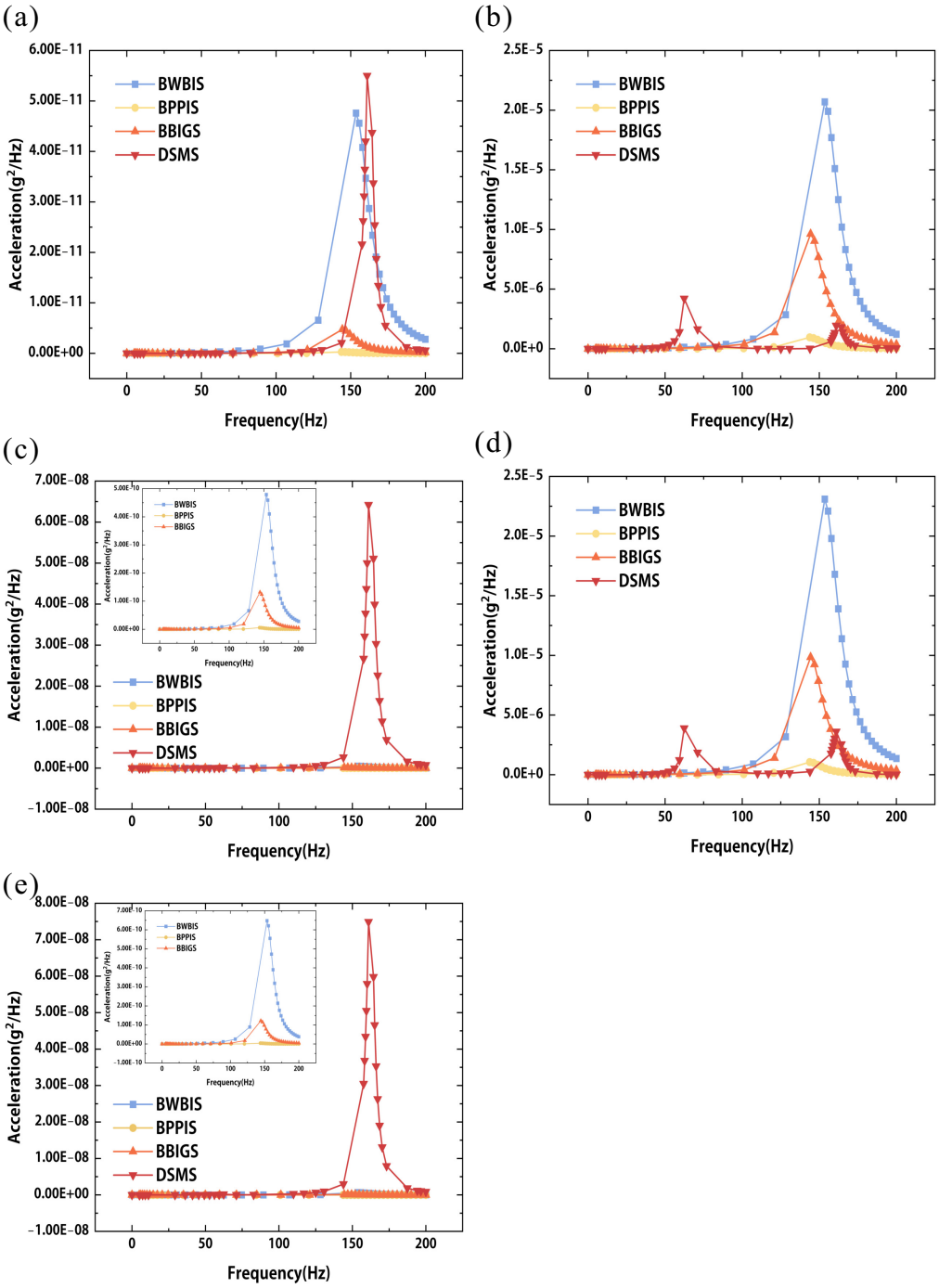

Figure 19. Transverse acceleration of the aluminum solid battery pack casing with different damping structures at (**a**) RP3, (**b**) RP8, (**c**) RP13, (**d**) RP18, and (**e**) RP23.

Table 6. The shock damping capability of the modified casings and damping structures in three directions.

Direction	Point	NHA (%)	NHA-BPPIS (%)	Auxetic (%)	Auxetic-BPPIS (%)
Vertical	RP 1	−86.41	−96.45	3.33	−109.55
	RP 2	−126.58	−149.44	−10.92	−136.49
	RP 3	−61.47	−66.61	19.95	−77.15
	RP 4	−62.37	−62.12	8.96	−88.51
	RP 5	−104.35	−50.62	−7.34	−146.17
Longitudinal	RP 11	16.03	85.47	21.40	84.83
	RP 12	12.43	75.83	−199.02	84.54
	RP 13	32.28	76.39	−56.50	81.19
	RP 14	−47.61	55.25	−269.77	71.68
	RP 15	45.35	74.79	−5.71	81.71
	RP 21	5.72	59.71	17.96	74.79
	RP 22	−38.35	50.21	−75.14	54.75
	RP 23	−13.76	32.53	−56.95	27.38
	RP 24	−44.49	−71.67	−124.44	−28.64
	RP 25	50.55	72.23	1.91	76.77
Transverse	RP 6	7.30	82.64	−1.62	86.17
	RP 7	25.48	22.95	3.29	90.18
	RP 8	26.60	35.09	8.82	87.64
	RP 9	20.51	68.74	19.56	84.59
	RP 10	−16.08	81.82	37.80	84.65
	RP 16	−9.62	82.15	5.00	87.02
	RP 17	−18.87	65.52	6.27	96.01
	RP 18	5.89	59.35	42.17	95.32
	RP 19	61.47	85.87	33.58	95.45
	RP 20	10.04	84.08	−2.88	88.20

Table 7. The longitudinal vibration damping capability of the modified battery pack casings and damping structures in three directions.

Direction	Point	NHA (%)	Solid-BPPIS (%)	X-Shaped-BPPIS (%)	Auxetic-BPPIS (%)	NHA-BPPIS (%)
Longitudinal	RP 11	21.66	90.15	43.91	8.20	1.09
	RP 12	10.98	88.58	24.94	3.44	−1.72
	RP 13	24.58	90.12	36.67	15.55	10.19
	RP 14	22.02	81.07	35.97	8.87	17.44
	RP 15	15.86	90.75	7.41	5.05	4.86
	RP 21	11.20	85.26	30.52	49.17	15.53
	RP 22	6.64	85.99	20.98	12.23	7.36
	RP 23	18.88	85.62	27.58	2.86	7.62
	RP 24	18.29	89.36	10.65	18.98	9.55
	RP 25	17.03	86.54	43.23	−16.31	−3.21

Table 8. The vertical vibration damping capability of the modified battery pack casings and damping structures in three directions.

Direction	Point	NHA (%)	Solid-BPPIS (%)	X-Shaped-BPPIS (%)	Auxetic-BPPIS (%)	NHA-BPPIS (%)
Vertical	RP 1	27.01	68.28	1.35	4.55	7.99
	RP 2	2.12	5.76	4.19	5.96	−2.80
	RP 3	12.99	30.50	2.06	3.40	7.83
	RP 4	−1.84	11.32	22.75	7.83	−0.34
	RP 5	14.50	18.25	9.93	6.78	12.16

Table 9. The transverse vibration damping capability of the modified battery pack casings and damping structures in three directions.

Direction	Point	NHA (%)	Solid-BPPIS (%)	X-Shaped-BPPIS (%)	Auxetic-BPPIS (%)	NHA-BPPIS (%)
Transverse	RP 6	16.64	75.10	−0.8	18.49	18.77
	RP 7	14.31	87.58	4.21	21.80	15.39
	RP 8	14.60	84.64	5.16	20.56	18.77
	RP 9	32.13	89.58	4.54	19.04	15.18
	RP 10	25.88	74.56	0.87	22.90	18.29
	RP 16	15.48	88.66	7.69	17.25	22.99
	RP 17	6.68	85.40	3.08	9.29	3.26
	RP 18	8.30	85.79	22.31	23.77	14.11
	RP 19	2.14	83.32	9.31	12.97	8.77
	RP 20	8.47	81.39	15.58	26.78	19.21

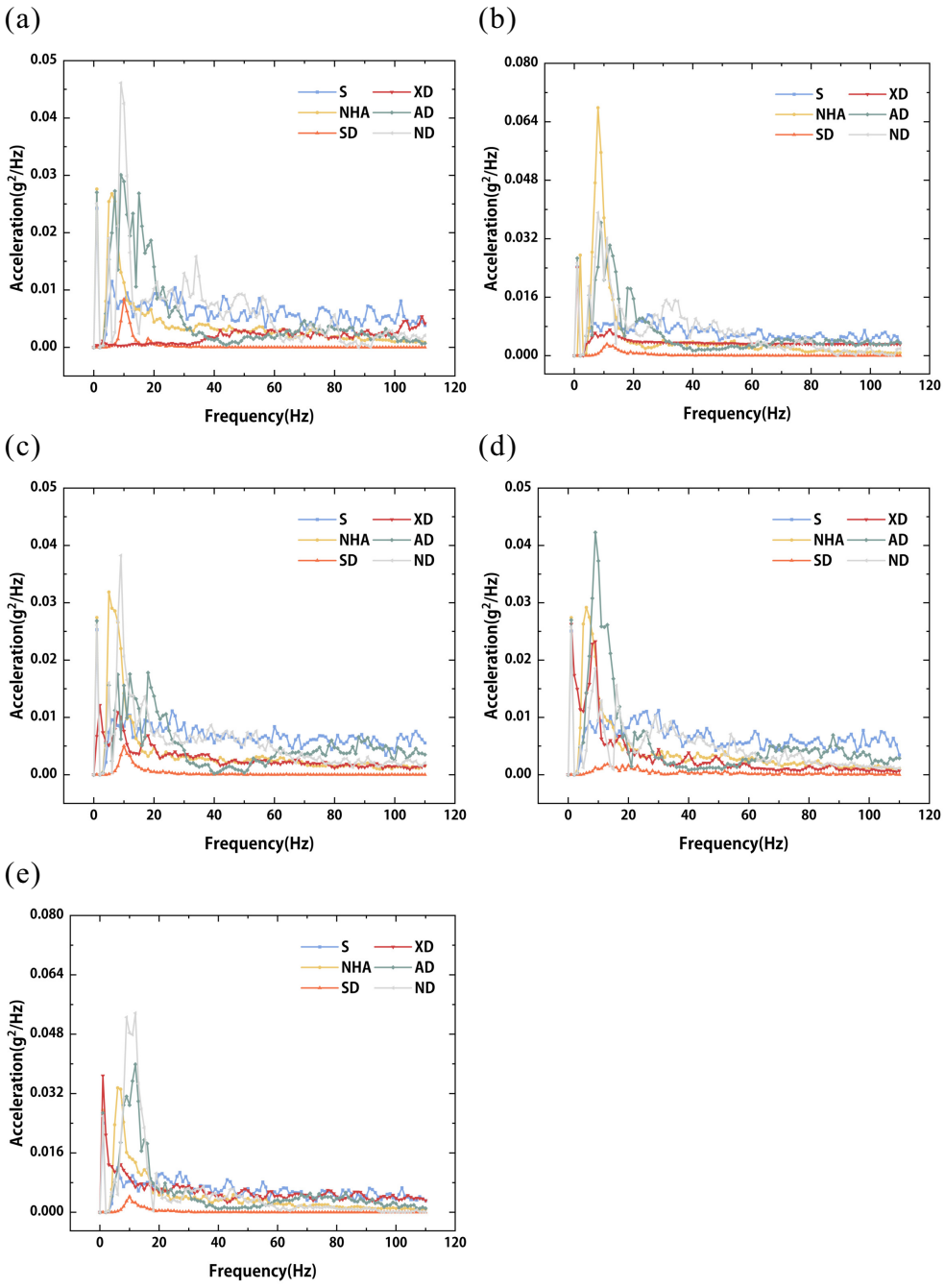

Figure 20. Longitudinal acceleration of the modified battery pack casings with BPPIS at (**a**) RP11, (**b**) RP12, (**c**) RP13, (**d**) RP14, and (**e**) RP15. S: solid, SD: solid with BPPIS, XD: X-shaped with BPPIS, AD: auxetic with BPPIS, ND: NHA with BPPIS.

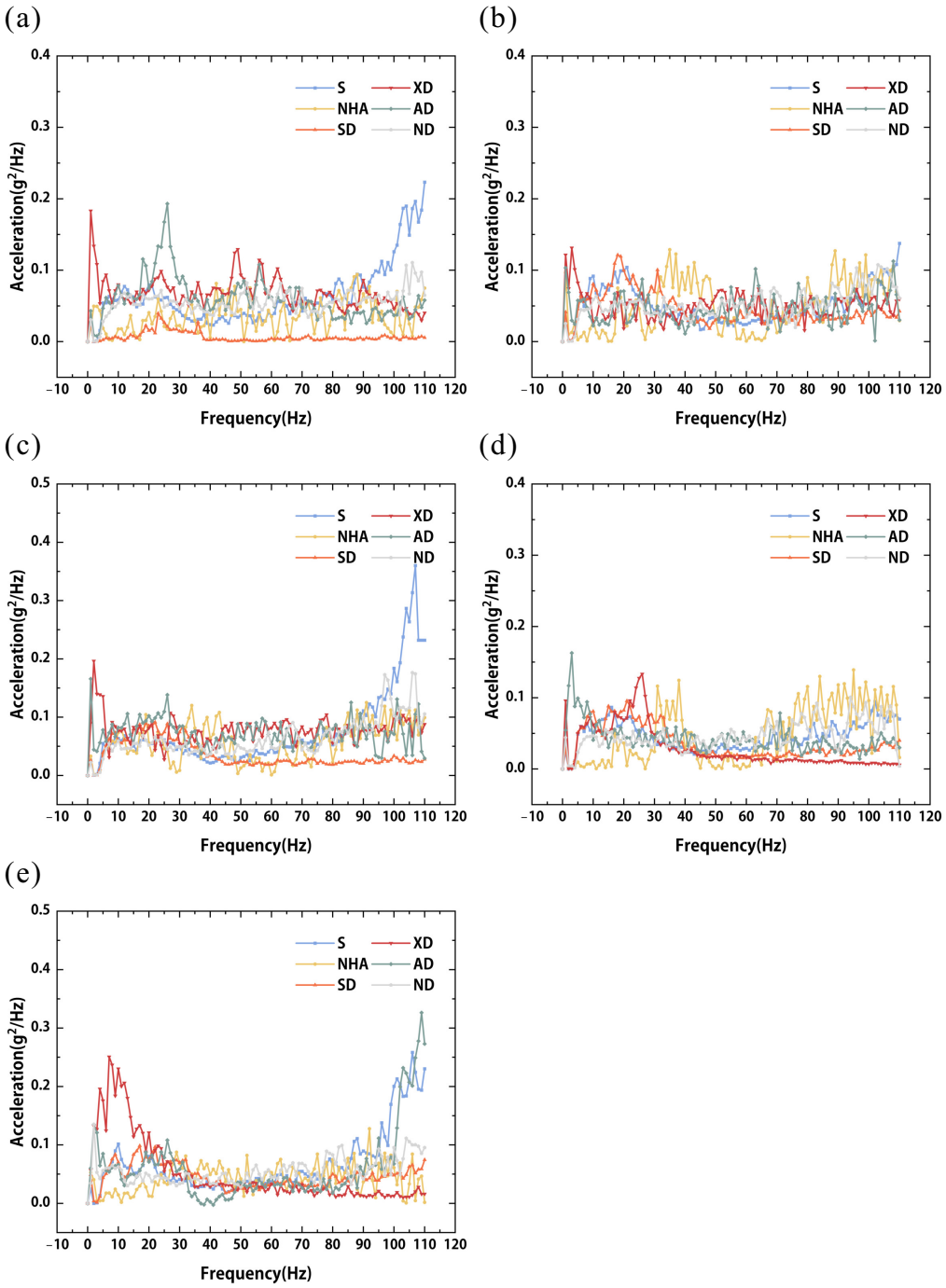

Figure 21. Vertical acceleration of the modified battery pack casings with BPPIS at (**a**) RP1, (**b**) RP2, (**c**) RP3, (**d**) RP4, and (**e**) RP5.

For the wall-modified designs, the performance becomes more direction- and location-dependent. The NHA wall modification (without BPPIS) provides moderate reductions on average—about 10.96%, 16.71%, and 14.46% in the vertical, longitudinal, and transverse directions, respectively—yet it is not uniformly beneficial, as vibration amplification is still observed at certain locations (e.g., vertical RP4, −1.84%). When the bottom damping is additionally introduced (NHA-BPPIS), the improvement is not guaranteed: although all transverse points remain positive (average 15.47%), multiple amplification points appear in the vertical and longitudinal directions (e.g., vertical RP2 −2.80%, RP4 −0.34%; longitudinal RP12 −1.72%, RP25 −3.21%), resulting in relatively limited averages of 4.97% (vertical) and 6.87% (longitudinal). This suggests that coupling between the wall compliance and

the bottom damping boundary condition may shift local mode shapes and redistribute dynamic loads, which can reduce the net attenuation at specific points.

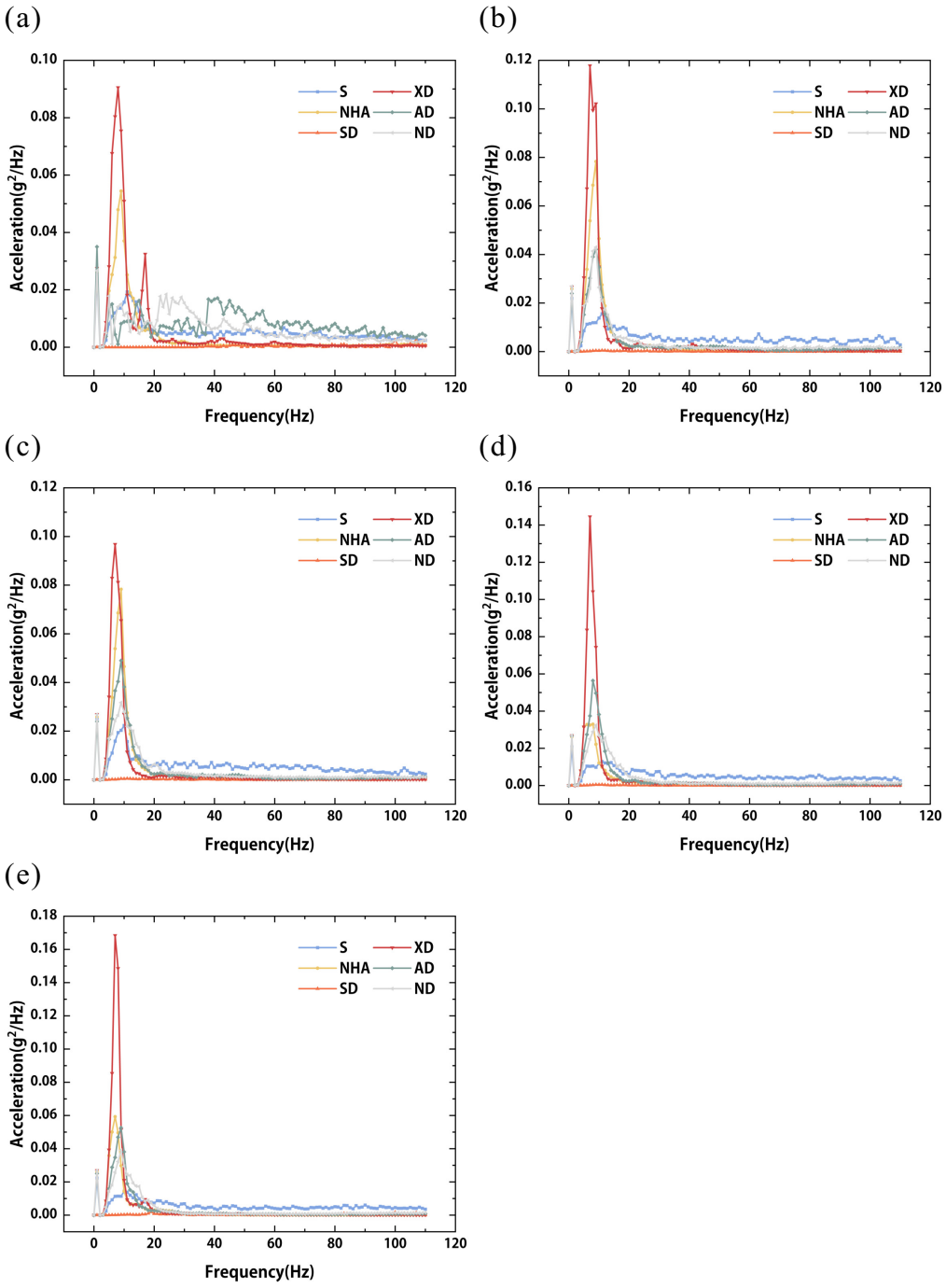

Figure 22. Transverse acceleration of the modified battery pack casings with BPPIS at (**a**) RP6, (**b**) RP7, (**c**) RP8, (**d**) RP9, and (**e**) RP10.

Comparing the two damped wall-modification candidates, X-shaped-BPPIS performs better in the longitudinal direction (average 28.19%) than auxetic-BPPIS (average 10.80%), while auxetic-BPPIS exhibits its strongest advantage in the transverse direction (average 19.29%, with a maximum of 26.78% at RP20). However, auxetic-BPPIS also shows a clear instability at certain locations (longitudinal RP25, −16.31%), indicating that the auxetic wall may introduce local resonant responses or unfavorable deformation patterns under longitudinal excitation, which can offset the benefit of the bottom damping. To achieve robust vibration mitigation across all measurement points, solid-BPPIS is the

most reliable configuration in this dataset. If wall modifications are required for additional objectives such as light-weighting or functional integration, the selection should be direction-specific: X-shaped-BPPIS is preferable for longitudinal mitigation, whereas Auxetic-BPPIS performs better in transverse mitigation but should be validated at critical locations due to potential amplification at certain points.

4. Conclusions

In this study, the vibration and shock mitigation performance of an aluminum battery pack casing is systematically evaluated through simulations and experiments, focusing on wall modifications (NHA, STH) and bottom damping configurations. To select a manufacturable damping solution for physical validation, four damping structure concepts (BPPIS, BWBIS, BBIGPS, and DSMS) are compared in simulation. Mechanistically, the four damping structures concepts exhibit distinct dissipation pathways. For BPPIS, the layered configuration establishes a spatial stiffness gradient that enables the front layer to absorb and diffuse the initial impact, while the intermediate and rear layers progressively deform and dissipate energy, thereby reducing peak responses and extending the duration of energy release. Moreover, the impedance mismatch and microslip at the interfaces between adjacent layers effectively attenuate vibration transmission and broaden the damping bandwidth, enabling synergistic control of broadband vibration and impact mitigation. For BWBIS, the sinusoidal superposition tailors the effective stiffness distribution and deformation pathways, facilitates progressive deformation and interfacial frictional dissipation, and consequently reduces peak response, leading to improved vibration attenuation and enhanced specific energy absorption.

For BBIGPS, the graded porous layered configuration similarly forms a spatial stiffness gradient, such that the front layer buffers and diffuses the initial impact and the subsequent layers deform sequentially to dissipate energy, which reduces peak responses and extends the energy-release duration. For DSMS, its quasi-zero stiffness feature helps to reduce the equivalent stiffness of the system under small-amplitude excitation and achieve vibration isolation. Meanwhile, under impact loads, significant nonlinear energy dissipation is triggered through the controllable buckling and snap-through buckling of the strips, thereby achieving impact energy dissipation and attenuation. BPPIS and BBIGPS provide superior mitigation relative to BWBIS and DSMS. BPPIS was finally selected for fabrication because it offers a simpler geometry and lower mass than BBIGPS.

The experimental data shows that under random vibration, solid-BPPIS provides the most robust and consistent attenuation across all measurement points, achieving average RMS reductions of 26.82% (vertical), 87.34% (longitudinal), and 83.60% (transverse), with positive reductions at every point. It should be noted that the experimental results in the present study are limited to 110 Hz and therefore cannot show some other important resonance features at higher frequencies. By comparison, the NHA wall modification without bottom damping yields moderate average reductions (10.96% vertical, 16.71% longitudinal, and 14.46% transverse) but remains location-dependent. Adding bottom damping to the NHA design does not guarantee further improvement, as amplification points appear in the vertical and longitudinal directions, resulting in limited averages of 4.97% (vertical) and 6.87% (longitudinal) despite maintaining positive transverse reductions (15.47% on average). Between the two wall-modification candidates that combined with bottom damping, X-shaped-BPPIS performs better in the longitudinal direction (28.19% on average), whereas Auxetic-BPPIS shows its strongest advantage in the transverse direction (19.29% on average) but may cause severe local amplification, highlighting the need for point-specific validation.

Shock tests further demonstrate that mitigation performance is strongly direction-dependent and can differ from random-vibration trends. Without additional damping structures, the auxetic casing shows better shock mitigation in the vertical and transverse directions, while the NHA casing performs better in the longitudinal direction. When damping structures are added, both designs show clear improvements in the longitudinal and transverse directions. In contrast, vertical shock mitigation remains limited, and the auxetic vertical capability decreases from 60% to 0% after adding the damping structure. The maximum shock mitigation is observed in the transverse direction, reaching 85.87% for NHA-damping and 96.01% for auxetic-damping. These results indicate that bottom damping and interface conditions primarily enhance transverse and longitudinal shock resistances, while vertical shock mitigation requires further design optimization.

It should be noted that the present study mainly focuses on the design-level evaluation of vibration and shock mitigation performance. Although the NHA casing and BPPIS damping structure are fabricated using aluminum 3D printing and experimentally validated under ISO 12405-2-based random vibration and shock conditions, long-term durability and fatigue resistance under realistic EV service environments are not fully investigated in this work. Therefore, the present results should be interpreted as short-term dynamic performance evidence rather than a direct prediction of long-term service life. Future work will include extended cyclic vibration tests, fatigue analysis, thermal-mechanical coupling, and durability evaluation under more representative road and environmental conditions.

Author Contributions: Conceptualization, H.P.L.; methodology, H.M.L.; software, Y.F. and B.Z.; validation, H.M.L.; formal analysis, Y.F. and B.Z.; investigation, Y.F. and B.Z.; resources, H.P.L.; data curation, Y.F. and B.Z.; writing—original draft preparation, Y.F.; writing—review and editing, H.M.L.; visualization, H.M.L.; supervision, H.P.L.; project administration, H.P.L. All authors have read and agreed to the published version of the manuscript.

Funding: This research/project is supported by RIE2020/RIE2025 <A*STAR IAFPP> (Award <M23L6a0020>), administered by A*STAR.

Data Availability Statement: Data are not available due to commercial restrictions from the funding agency.

Conflicts of Interest: The authors declare no conflicts of interest.

Appendix A

Table A1. PSD profile of the x-longitudinal step [35].

Frequency (Hz)	PSD (g^2/Hz)
5	0.0125
10	0.03
20	0.03
200	0.00025

Table A2. PSD profile of the y-vertical step [35].

Frequency (Hz)	PSD (g^2/Hz)
5	0.05
10	0.06
20	0.06
200	0.0008

Table A3. PSD profile of the z-transverse step [35].

Frequency (Hz)	PSD (g^2/Hz)
5	0.01
10	0.015
20	0.015
50	0.01
200	0.0004

Table A4. Mechanical shock test-parameters [35]. RT is the room temperature.

Procedure	Requirement
Pulse shape	half-sinusoidal
Acceleration	500 m/s^2
Duration	6 ms
Temperature	RT
Number of shocks	10 per test direction

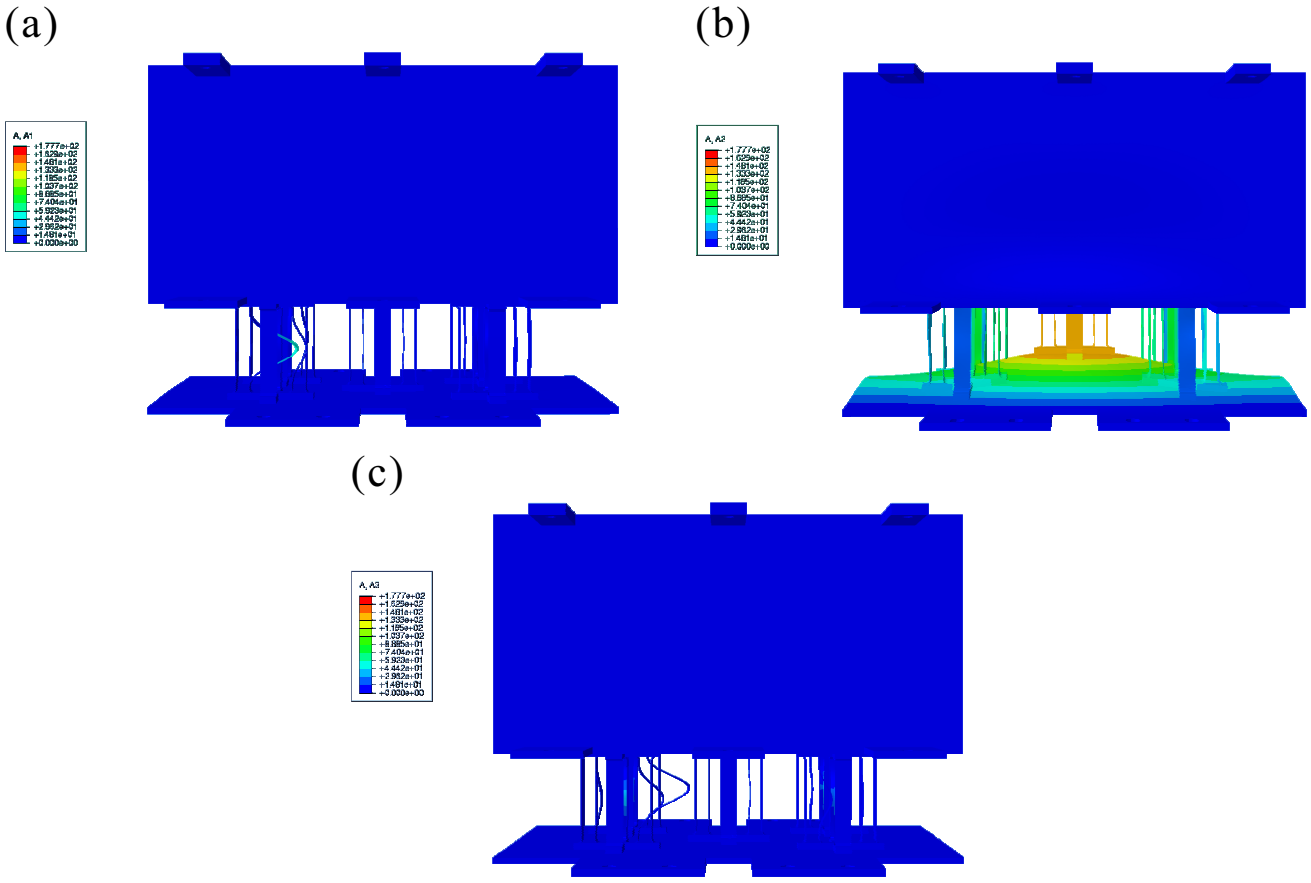

Figure A1. Acceleration contours of the aluminum solid battery pack casing with attached DSMS in (**a**) longitudinal (152 Hz), (**b**) vertical (50 Hz) and (**c**) transverse (160 Hz) directions.

References

1. Arora, S.; Shen, W.; Kapoor, A. Review of mechanical design and strategic placement technique of a robust battery pack for electric vehicles. *Renew. Sustain. Energy Rev.* **2016**, *60*, 1319–1331. [CrossRef]
2. Awan, U.S.; Ghabraie, K.; Zolfagharian, A.; Whimpey, S.; Rolfe, B. Understanding batteries integration in EV structure: Trade-offs and optimization. *J. Energy Storage* **2026**, *148*, 120289. [CrossRef]
3. Hooper, J.M.; Marco, J. Characterising the in-vehicle vibration inputs to the high voltage battery of an electric vehicle. *J. Power Sources* **2014**, *245*, 510–519. [CrossRef]
4. Kadic, M.; Milton, G.W.; van Hecke, M.; Wegener, M. 3D metamaterials. *Nat. Rev. Phys.* **2019**, *1*, 198–210. [CrossRef]

5. Lee, J.H.; Singer, J.P.; Thomas, E.L. Micro-/Nanostructured Mechanical Metamaterials. *Adv. Mater.* **2012**, *24*, 4782–4810. [CrossRef]
6. Huang, C.; Chen, L. Negative Poisson's Ratio in Modern Functional Materials. *Adv. Mater.* **2016**, *28*, 8079–8096. [CrossRef] [PubMed]
7. Jiang, L.; Hu, H. Low-velocity impact response of multilayer orthogonal structural composite with auxetic effect. *Compos. Struct.* **2017**, *169*, 62–68. [CrossRef]
8. Gibson, L.J.; Ashby, M.F.; Schajer, G.S.; Robertson, C.I. The mechanics of two-dimensional cellular materials. *Proc. R. Soc. Lond. Ser. A Math. Phys. Sci.* **1982**, *382*, 25–42. [CrossRef]
9. Larsen, U.D.; Sigmund, O.; Bouwstra, S. Design and fabrication of compliant micromechanisms and structures with negative Poisson's ratio. *J. Microelectromech. Syst.* **1997**, *6*, 99–106. [CrossRef]
10. Grima, J.N.; Gatt, R.; Alderson, A.; Evans, K.E. On the potential of connected stars as auxetic systems. *Mol. Simul.* **2005**, *31*, 925–935. [CrossRef]
11. Han, D.; Li, P.; Li, P.; Li, L.; Bai, C.; Fan, H.; Wang, P.; Song, Z.; Yang, F. Utilizing partially-curved-beam to improve stress response and energy absorption performance of auxetic lattice metamaterials. *Thin-Walled Struct.* **2025**, *217*, 113896. [CrossRef]
12. Jiao, P.; Mueller, J.; Raney, J.R.; Zheng, X.R.; Alavi, A.H. Mechanical metamaterials and beyond. *Nat. Commun.* **2023**, *14*, 6004. [CrossRef] [PubMed]
13. He, X.; Li, G.; Zhang, L.; Huang, Y.; Xie, B.; Shi, Z.; Feng, G.; Liu, W.; Lyu, F.; Wang, S.; et al. Bio-inspired material-structure-function integrated additive manufacturing of Al-based metamaterials with surpassing energy absorption. *Sci. Adv.* **2025**, *11*, eaea0430. [CrossRef]
14. Jiang, J.; Wang, H.; Lin, J.; Wang, F.; Liu, Z.; Wang, L.; Li, Z.; Li, Y.; Li, Y.; Lu, Z. Nature-inspired hierarchical building materials with low CO2 emission and superior performance. *Nat. Commun.* **2025**, *16*, 3018. [CrossRef] [PubMed]
15. Hou, Y.; Peng, Y.; Li, P.; Wu, Q.; Zhang, J.; Li, W.; Zhou, G.; Wu, J. Bioinspired Design of High Vibration-Damping Supramolecular Elastomers Based on Multiple Energy-Dissipation Mechanisms. *ACS Appl. Mater. Interfaces* **2022**, *14*, 35097–35104. [CrossRef]
16. Li, X.; Yu, X.; Zhao, M.; Li, Z.; Wang, Z.; Zhai, W. Multi-Level Bioinspired Microlattice with Broadband Sound-Absorption Capabilities and Deformation-Tolerant Compressive Response. *Adv. Funct. Mater.* **2023**, *33*, 202210160. [CrossRef]
17. Silva, L.T.; Magalhaes, A.; Silva, J.F.; Fonseca, F. Impacts of low-frequency noise from industrial sources in residential areas. *Appl. Acoust.* **2021**, *182*, 108203. [CrossRef]
18. Wei, Q.; Han, H.; Lee, H.M.; Lee, H.P. Design of the vibration damping structures for battery pack casing of an electric vehicle. *Mech. Syst. Signal Process.* **2025**, *238*, 113253. [CrossRef]
19. Wei, L.; Zhao, X.; Yu, Q.; Zhu, G. Quasi-static axial compressive properties and energy absorption of star-triangular auxetic honeycomb. *Compos. Struct.* **2021**, *267*, 113850. [CrossRef]
20. Yan, S.; Wu, L.; Meng, Z.; Tan, X.; Liu, W.; Wen, Y.; Sun, J.; Tian, X.; Zhou, J. Double-strip metamaterial for vibration isolation and shock attenuation. *Int. J. Mech. Sci.* **2024**, *282*, 109686. [CrossRef]
21. Zhang, J.h.; Dong, B.j.; He, B.; Sun, Y. Free Vibrations and Impact Resistance of a Functionally Graded Honeycomb Sandwich Plate. *Shock Vib.* **2021**, *2021*, 8043368. [CrossRef]
22. Zhang, W.; Yu, T.X.; Xu, J. Uncover the underlying mechanisms of topology and structural hierarchy in energy absorption performances of bamboo-inspired tubular honeycomb. *Extrem. Mech. Lett.* **2022**, *52*, 101640. [CrossRef]
23. Wu, H.; Fan, G. An overview of tailoring strain delocalization for strength-ductility synergy. *Prog. Mater. Sci.* **2020**, *113*, 100675. [CrossRef]
24. Ding, Z.; Wang, B.; Xiao, H.; Duan, Y. Hybrid Bio-Inspired Structure Based on Nacre and Woodpecker Beak for Enhanced Mechanical Performance. *Polymers* **2021**, *13*, 3681. [CrossRef]
25. Zhang, J.; Meng, S.; Wang, B.; Xu, Y.; Shi, G.; Zhou, X. Bio-Inspired Sinusoidal Metamaterials: Design, 4D Printing, Energy-Absorbing Properties. *Machines* **2024**, *12*, 813. [CrossRef]
26. Zhou, J.; Zou, M.; Ng, B.F.; Ou, M. Emerging sinusoidal structures for energy absorption: Mechanisms, optimizations and applications. *Compos. Part B: Eng.* **2025**, *306*, 112759. [CrossRef]
27. Yu, Z.; Liu, J.; Wei, X. Achieving outstanding damping performance through bio-inspired sutural tessellations. *J. Mech. Phys. Solids* **2020**, *142*, 104010. [CrossRef]
28. Dormohammadi, R.; Farzaneh-Gord, M.; Ebrahimi-Moghadam, A.; Ahmadi, M.H. Heat transfer and entropy generation of the nanofluid flow inside sinusoidal wavy channels. *J. Mol. Liq.* **2018**, *269*, 229–240. [CrossRef]
29. Wen, Z.; Sha, Y.; Yu, T.X.; Jun, X. Crushing resistance and energy absorption of pomelo peel inspired hierarchical honeycomb. *Int. J. Impact Eng.* **2019**, *125*, 163–172. [CrossRef]
30. Bustihan, A.; Hirian, R.; Botiz, I. Reusable 3D-Printed Thermoplastic Polyurethane Honeycombs for Mechanical Energy Absorption. *Polymers* **2025**, *17*, 3035. [CrossRef]
31. Lin, K.; Gu, D.; Hu, K.; Yang, J.; Wang, H.; Yuan, L.; Shi, X.; Meng, L. Laser powder bed fusion of bio-inspired honeycomb structures: Effect of twist angle on compressive behaviors. *Thin-Walled Struct.* **2021**, *159*, 107252. [CrossRef]

32. Guo, W.; Yang, L.; Xu, P.; Li, S.; Yan, W.; Shen, Z.; Yao, S.; Yang, C. Crashworthiness analysis of okra biomimetic corrugated multi-cellular structure. *Int. J. Mech. Sci.* **2024**, *280*, 109459. [CrossRef]
33. YingboMetal. Available online: https://shanxiyingbo.com/productinfo/1384058.html (accessed on 10 June 2026).
34. Lee, H.M.; Lee, H.P. Mechanical Metamaterials in Mitigating Vibrations in Battery Pack Casings. *Energies* **2025**, *18*, 2114. [CrossRef]
35. *ISO 12405-4:2018*; Electrically Propelled Road Vehicles—Test Specification for Lithium-Ion Traction Battery Packs and Systems—Part 4: Performance Testing. ISO: Geneva, Switzerland, 2018; Edition 1; 72p.
36. STTAi. DC Series Basic Electro-Dynamic Shaker (Air-Cooled). Online Product Page. Available online: https://www.chinasti.com/ (accessed on 5 May 2025).
37. Gröhlich, M.; Lang, A.; Böswald, M.; Meier, J. Viscoelastic damping design–Thermal impact on a constrained layer damping treatment. *Mater. Des.* **2021**, *207*, 109885. [CrossRef]
38. Jaisee, S.; Yue, F.; Ooi, Y.H. A state-of-the-art review on passive friction dampers and their applications. *Eng. Struct.* **2021**, *235*, 112022. [CrossRef]

Disclaimer/Publisher's Note: The statements, opinions and data contained in all publications are solely those of the individual author(s) and contributor(s) and not of MDPI and/or the editor(s). MDPI and/or the editor(s) disclaim responsibility for any injury to people or property resulting from any ideas, methods, instructions or products referred to in the content.